Title Page

Atomistic simulation study of the transformation mechanisms of γ and ε phases from α-Fe single crystal during the crack propagation process

Zheng Wang[a], Xiaoming Shi[a], Xu-Sheng Yang[b,d], Wangqiang He[a], San-Qiang Shi[c]**, Xingqiao Ma[a]*

a. Department of physics, University of Science and Technology Beijing, Beijing, China

b. Advanced Manufacturing Technology Research Centre, Department of Industrial and Systems Engineering, The Hong Kong Polytechnic University, Hung Hom, Kowloon, Hong Kong, China

c. Department of Mechanical Engineering, The Hong Kong Polytechnic University, Hung Hom, Kowloon, Hong Kong, China

d. Hong Kong Polytechnic University Shenzhen Research Institute, Shenzhen 518057, China

Zheng Wang, email: tomwangsim@163.com
ORCID: 0000-0002-0621-3678
Xiaoming Shi, email: shiming_870@163.com
ORCID: 0000-0001-7332-6835
Xu-Sheng Yang, email: xsyang@polyu.edu.hk
ORCID: 0000-0003-0769-778X
Wangqiang He, email: hewangqiang@yeah.net
ORCID: 0000-0001-9717-7205
San-Qiang Shi**, Corresponding author, email: san.qiang.shi@polyu.edu.hk
ORCID: 0000-0003-4189-0786

Xingqiao Ma*, Corresponding author, email: xqma@sas.ustb.edu.cn

ORCID: 0000-0001-9718-1538

Atomistic simulation study of the transformation mechanisms of γ and ε phases from α-Fe single crystal during the crack propagation process

Zheng Wang[a], Xiaoming Shi[a], Xu-Sheng Yang[b,d], Wangqiang He[a], San-Qiang Shi[c**], Xingqiao Ma[a*]

a. Department of physics, University of Science and Technology Beijing, Beijing, China
b. Advanced Manufacturing Technology Research Centre, Department of Industrial and Systems Engineering, The Hong Kong Polytechnic University, Hung Hom, Kowloon, Hong Kong, China
c. Department of Mechanical Engineering, The Hong Kong Polytechnic University, Hung Hom, Kowloon, Hong Kong, China
d. Hong Kong Polytechnic University Shenzhen Research Institute, Shenzhen 518057, China

Abstract

Strain-induced martensitic transformations have been widely observed in pure iron and iron alloys under various mechanical loading conditions, thereby showing extreme scientific merits and engineering significance. However, a deep understanding of the martensitic transformations in α (bcc)-Fe single crystal under tension conditions is still quite limited. In this work, the molecular dynamics (MD) simulation and first-principle calculations were performed to study the crack propagation process of α-Fe single crystal with a (010)[100] pre-crack under tension along the [010] direction. An algorithm for tracking the crack tip by scanning nearby atoms was proposed in the MD simulation to obtain the critical stress intensity factor, which is proved to be close to the experimental results. Simulation results show that the fracture process is the quasi-cleavage fracture, and its microscopic plasticity is found to be attributed to the nucleation and growth of the γ (fcc) and ε (hcp) phases during the crack propagation. Specifically, the transformation mechanisms are revealed that γ phase is transformed by the shearing action of {121}<111> and {110}<111> slip systems of α phase near the crack tip, while the formation of ε phase with layered structure is resulted from the stacking faults inside of pre-transformed γ phase. Moreover, thermodynamic theory based on the volume change and shearing is applied to analyze the driving forces of such phase transformations, indicating that the ε phase is not stable due to rapid decreasing of the driving force in γ→ε phase transformation.

*Corresponding author. Department of physics, University of Science and Technology Beijing, Beijing, China
Email Address: xqma@sas.ustb.edu.cn (Xingqiao Ma)
** Corresponding author. Department of Mechanical Engineering, The Hong Kong Polytechnic University, Hung Hom, Kowloon, Hong Kong, China
Email Address: san.qiang.shi@polyu.edu.hk (Sanqiang Shi)

Keywords:
Strain-induced martensitic transformation; microscopic plasticity; α-Fe single crystal; fracture; atomistic simulation

1.Introduction

Most of the allotropic transformations in iron under external mechanical loading belong to the deformation-induced martensitic transformations (DIMTs), which is a rather common phenomenon and a diffusionless phase transition in crystalline solids. DIMT plays a pivotal role in the microstructural evolution and plasticity of iron and iron alloys, as well as many other types of engineering metals. As early as 1924, it was found that the softening phenomenon would happen in iron under mechanical loading at elevated temperatures [1, 2]. It might be attributed to the DIMTs, as evidenced later by transformations between body-centered cubic (bcc) phase and face-centered cubic (fcc) phase under tensile loading at about 910^{o}C [3] and the transformation of bcc phase to hexagonal close-packed (hcp) phase under high-pressure loading [4, 5], respectively, in pure iron and iron alloys. In addition, this phenomenon has also been observed in ferronickel alloys, shape memory alloys and even some Zr-based ceramics [1], etc.

Assisted by the shear stress and shear from deformation, γ phase in iron alloys can undergo transformations at a temperature between the martensitic transformation temperature M_s and the deformation-induced martensitic transformation temperature M_d, usually resulting in the $\gamma \rightarrow \alpha$ or $\gamma \rightarrow \varepsilon$ phase transformations [1, 7, 8]. The mechanisms of many of the above DIMTs are consistent with the model proposed by Olson and Cohen [6, 9–11], which have been experimentally verified and observed in AISI 304 austenite stainless steel by using high-resolution transmission electron microscopy (HRTEM) [12–14]. DIMT can cause the often observed TRansformation-Induced Plasticity (TRIP) effect [1, 7, 8, 15, 16]. When DIMT occurs, the hard martensite particles can effectively impede further plastic deformation locally, which continues exclusively in the regions containing the relatively soft unmodified austenitic phase. As a result, the deformation process becomes more homogeneous, thus enhancing the plasticity and strain-hardening properties of the material (i.e., the TRIP effect), and achieving the optimal combination of strength and ductility. Austenitic stainless steel [17–19], duplex and multiphase steel [20–25], and TRIP steels with Mn-Si components [26–28], etc, have been manufactured based on the above mechanism for the wide applications in the industry. In particular, it can provide thinner and lighter materials without losing the safety, reliability and mechanical properties, thus saving energy and cost, reducing difficulties during materials processing and use. Noticeably, the reverse transformation of γ phase from pre-transformed α phase could also be found in

TRIP materials with γ→α transformation, which has great benefits for grain refinement [19].

The α→ε phase transformation, which relates to the structure of the earth's inner core, has been extensively studied, especially by the in-situ experimental observations in 2005 [30, 31]. The anisotropy of the earth's inner core is also considered as a result of the formation of ε phase by plastic deformation of grains with preferred orientation during the solidification. The observed orientation relationship (OR) between α and ε phases was in accordance with that proposed by Burgers et al [5, 32–34]. Johnson et al have proposed a multiscale model based on the first-principle theory [35], showing that the required energy along the non-adiabatic shearing path is lower than that proposed in Burgers' model. By using the first-principle calculations, Lu et al proposed that α→ε phase transformation can be directly realized without the γ intermediate phase [36], via simultaneously shearing and reducing the interplanar distance of (110)α planes. In addition, they also pointed out the previously observed γ intermediate phase during the α→ε phase transformation in high-pressure MD simulation [37, 38] might be induced by the deviation in semi-empirical potentials.

Different from conditions of the MD simulation of impact processes, the α→γ phase transformation in iron is rarely observed under normal experimental conditions of mechanical loading [39, 40]. By using TEM and three-dimensional atomic probe tomography (3D APT), Ivanisenko et al for the first time observed the shear induced α→γ DIMT in pearlite steel during its severe plastic deformation induced-nanocrystallization process[41]. Later, in-situ X-ray diffraction (XRD) observations of the α→γ phase transformation in pure Fe and Fe-Au alloys were achieved in 2015 [42]. Theoretically, the required shearing action during the martensitic transformation could be activated from either uniaxial compression or uniaxial tension. The α→γ phase transformation under tensile loading along a single axis could also be possible in small-size systems. Because of the small energy difference between the γ phase and ε phase in iron [43], the existence of γ and ε phases in α matrix materials is often not well-distinguished in MD simulation, especially during tensile loading process [44–46]. Therefore, the transformation mechanisms (including the nucleation, growth, and atomic shear movements) of γ, ε phases from α phase, and their effects on the mechanical properties of materials need to be further studied. In this paper, we studied the detailed phase transformation process and mechanisms in α-iron single crystal during mode I fracture process under tension along the [010] direction, by using MD simulation and first-principle calculations.

2. Simulation and Modeling methods

2.1 Tensile loading of the specimen - MD simulations

MD simulations (Lammps software with embedded atom method (EAM) interatomic potential for iron

[49, 50]) were used to conduct the mode I fracture process of an α-Fe single crystal specimen with a (010)[100] pre-crack under quasi-static tension along [010] direction. For tracking the crack tip, we proposed a simple algorithm by scanning the atoms near the crack tip. Based on such algorithm, the stress intensity factor (SIF) at the crack tip can be calculated by using the extrapolation method. As depicted in Fig. 1(a), the specimen with size of 31.2nm (W) × 31.59nm (L) × 3.6nm (B) and about 300000 iron atoms was generated by periodically stacked α-Fe cells with a lattice constant of 2.866 Å. A narrow half elliptical pre-crack was created with a crack length of 10.8 nm (marked as a), and a crack opening of 0.86 nm (marked as b). After placing and fixing the specimen, the whole system was relaxed for 15 ps at 300 K using an isothermal isobaric ensemble (NPT). Then, mode I fracture process of the specimen was conducted along [010] direction at temperature of 300 K with a deformation rate about $3.1\times10^{8}s^{-1}$. The whole simulation took 450 ps with the time step of 0.1 fps.

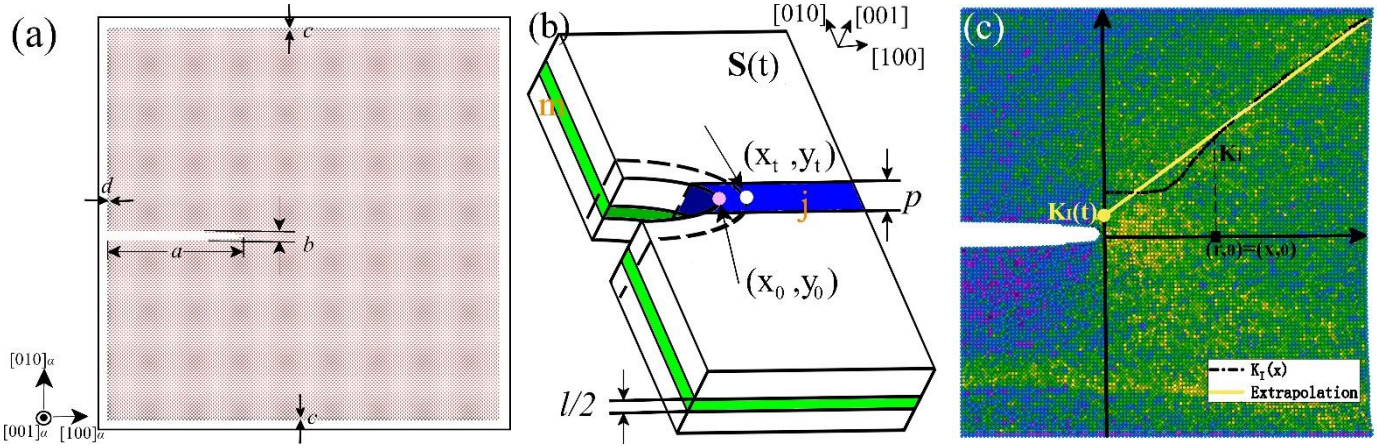

Fig. 1. Tensile loading model of α-Fe single crystal. (a) crystal structure and crack orientation, the specimen is modeled by extending periodically the cell of α-Fe along [100], [010], [001] directions to form a thin sheet with a half elliptical pre-crack. (b) the simple algorithm for tracking crack tip, layered specimen along [001] and [010] directions to find out the nearest atoms to previous position of the crack tip. (c) extrapolation for SIF calculation, $K_I(x)$ is obtained from far away to near the crack tip along crack extension direction, then extrapolates to the crack tip.

Visualization software Ovito [59] was used to identify dislocations, phase transformation and shear strain. The virtual selected-area electron diffraction (SAED) method [63, 64] was used to identify ORs between different phases. When SAED calculation was carried out, the electron radius was set to 0.0251 Å, which was equivalent to the operating voltage of 200 kV of TEM, and results was graphed by VisIt [65]. For obtaining the distance between γ phase and the crack tip, and the angular relationship between γ phase and crack propagation direction, the ConvexHull module [66] of SciPy [62] was used. With this method the projected convex polygon by different regions' atoms of γ phase formed in the (001)α plane has been firstly obtained, and then the coordinates of the center point was found out. After that, the distance and angle could be

calculated through the vectors' rules. In this work, the phase transition and dislocation recognition region were confined to the radius of 50 Å in front of the crack tip.

In this work, we proposed a simple algorithm for tracking crack tip along its extension direction by scanning nearby atoms. As depicted in Fig. 1(b), we first assume the original coordinate of the crack tip is (x_0, y_0), and the transient loaded structure at time of *t* is **S**(t), where the thicknesses of M layers along the [001]α direction is half lattice constant (*l*/2) and J layers along [010]α direction is *p* = 1.5Å, less than the size of **S**(t) along [010]α divided by stacked periods. Then, M layers are scanned by each layer to find out the *j*-th layer which ensures max ($y_{m,j}$)>y_0≥min ($y_{m,j}$) along [010]α direction in the *m*-th layer in [001]α direction. In addition, finding out the $x_{m,j}$ to make sure min($x_{m,j}$-x_0)and the nearest position to crack tip in the *m*-th layer is ($x_{m,j}$,$y_{m,j}$). So, the position of the crack tip at time *t* is (x_t,y_t)=(<$x_{m,j}$>,<$y_{m,j}$>), which is the average position of ($x_{m,j}$,$y_{m,j}$) for the M layers. Finally, the position of the crack tip for the next time step can be calculated after replacing (x_0,y_0) with the above value.

The normal stress σ_{yy} of each atom in the *j*-th layer can be determined after the crack tip position is obtained. As shown in Fig. 1(c), the value of SIFis averaged at the same distance from the crack tip. Then the SIF at the crack tip at time *t* ($K_{I,tip}(t)$) can be calculated directly by using extrapolation method based on its definition [73–75]:

$$\begin{aligned} K_I(r,t) &= \sqrt{2\pi r}\sigma_{yy}(r,\theta{=}0,t) \\ K_{I,tip}(t) &= \lim_{r\to 0} K_I(r,t) \end{aligned} \tag{1}$$

The critical SIF of mode I fracture (K_{IC}) is the maximum of $K_{I,tip}(t)$:

$$K_{IC} = \max[K_{I,tip}(t)] \tag{2}$$

Atomic stress is calculated according to the following formula [76]:

$$\sigma_i = \frac{1}{\Omega_i}\left(m_i v_i \otimes v_i + \sum_{j\neq i} r_{i,j} \otimes f_{i,j} \right) \tag{3}$$

Ω_i is the volume of the Voronoi polyhedral calculated by Lammps with Voro++ Quickhull Algorithm Library [66]. m_i is the mass of the atom, v_i is atomic velocity. $\mathbf{r}_{i,j}$ and $\mathbf{f}_{i,j}$ represent the relative position vector and force between atoms *i* and *j*, respectively.

Stress of each phase, σ, can be obtained by average atomic stresses, according to the definition of stress invariants[77]:

$$
\begin{aligned}
I_1 &= \sigma_{xx} + \sigma_{yy} + \sigma_{zz} \\
I_2 &= \begin{vmatrix} \sigma_{yy} & \tau_{yz} \\ \tau_{zy} & \sigma_{zz} \end{vmatrix} + \begin{vmatrix} \sigma_{zz} & \tau_{zx} \\ \tau_{xz} & \sigma_{xx} \end{vmatrix} + \begin{vmatrix} \sigma_{xx} & \tau_{xy} \\ \tau_{yx} & \sigma_{yy} \end{vmatrix} \\
I_3 &= \begin{vmatrix} \sigma_{xx} & \tau_{xy} & \tau_{xz} \\ \tau_{yx} & \sigma_{yy} & \tau_{yz} \\ \tau_{zx} & \tau_{zy} & \sigma_{zz} \end{vmatrix}
\end{aligned} \tag{4}
$$

The hydrostatic stress σ_{hyd}, the maximum principal stress σ_{max} and maximum shear stress τ_{max} can be calculated by using formulas:

$$
\begin{aligned}
&\sigma^3 - I_1\sigma^2 + I_2\sigma - I_3 = 0 \\
&\sigma_{max} = \max(\sigma) \\
&\tau_{max} = \frac{1}{2}(\max(\sigma) - \min(\sigma)) \\
&\sigma_{hyd} = \bar{\sigma}
\end{aligned} \tag{5}
$$

2.2 Modeling for phase stability and fracture—first-principle calculations

During the whole tension process of iron specimen, γ and ε phases are found to be transformed with a certain OR. Therefore, we designed five structural evolution paths in first-principle calculations to understand the stability of transited phase and discuss the relationship between fracture and phase transition observed in the MD simulation. All models were constructed by using the Vienna Ab-initio Simulation Package (VASP)[78–81], and the generalized gradient approximation (GGA) proposed by Perdew, Burke and Ernzerhof was used to describe the electron exchange correlation with spin polarization [82, 83]. The electron-ion interaction was described by the augmented plane wave method (PAW) [84, 85]. Truncation energy of the plane wave was set to 450 eV. K points were generated in the Monkhorst-Pack mode [86], and the number of K points in irreducible Brillouin zone was generated by vaspkit [87]. It had been tested to ensure that the convergence of the total energy was better than that of 3 meV/atom. The average total energy per atom and volume relationships (E-V) of iron α, γ and ε were calculated with the same settings before the model was solved. The equilibrium lattice constants of these phases were obtained by fitting the equation of state proposed by Birch and Murnaghan [88, 89]. (是否考虑简化这段描述？)

Five paths defined in this work are denoted as P1, P2, P3, P4, and P5, respectively, as the atomic structures depicted in Fig. 2, where the original lengths, *L*, of matrix lattices are transited to *L'* along the deformation directions. More specifically, five calculation paths were set as follows: (可否考虑简化五种路径的描述？)

P1 adopts the structure shown in Fig. 2(a), where *L* was uniformly changed along three base directions of the unit cell. Averaged atomic energy E_{P1} of the system was calculated with the ferromagnetism (FM) magnetic

state constructed by arranging the spin of all atom layers as …↑↑↑…along the [010]α direction initially. The generated set of K points used in this path is 12×12×12.

P2 adopts the structure shown in Fig. 2(b), in which five unit cells were stacked along the [100]α direction to construct a supercell with FM magnetic state and the initial spin arranging as …↑↑↑… along the same direction. The structure was fixed along [010]α, and relaxed along [100]α and [001]α directions to gradually change length *L*. The generated set of K points is 2×9×9. This path was used to present the fracture occurred in the middle cell, and then the average atomic energy E_{P2} of the fracture portion could be obtained.

Path P3 describes the possible path of an α→γ phase transformation. As shown in the right part of Fig. 2(c), Bain OR [90] was used in the calculation, i.e., (010)α//(010)γ and [100]α//[101]γ. P3 path was divided into two processes, i.e., the P3 FM with the initial spin configuration as ⋯↑ ↑ ↑ ↑⋯ along the [010]α direction, and the P3 AFMD with initial spin configuration as ⋯↑ ↑ ↓ ↓ ↑ ↑ ↓ ↓⋯ along the [010]α direction, respectively. As depicted in the upper left part of Fig. 2(c), the P3 FM used the unit cell as its initial structure. *L* was changed along the [010]α direction and other two directions were relaxed in this path. The generated set of K points is 9×5×9 and the average atomic energy E_{P3F} was calculated with the atomic spin along [010]α. The E_{P3A} of P3 AFMD was calculated based on the structure depicted in the lower left part of Fig. 2(c), where the length of the entire structure was changed along the [010]α direction with the relaxation along other two directions. The generated set of K points is 9×5×9. The structural variable *L* was chosen to be half length along the [010]α direction, and magnetic state was set to AFMD [91] along the [010]α direction.

According to the Burgers model, OR between the orthogonalized hcp ε cell and a bcc α cell satisfied [010]α//[$\bar{1}2\bar{1}0$]ε and (101)α//(0001)ε, as shown in the lower part of Fig. 2(d). So, the path P4 structure was set to an hcp orthogonalized unit cell depicted in the upper part of Fig. 2(d), which was a part of an hcp conventional cell. In P4 path, the magnetic statement was set to the non-magnetic (NM) state [96], while the lattice constant *L* was tensioned and then fixed many times along the [010]α direction. The generated set of K points is 7×13×7. The average atomic energy E_{P4} was calculated after relaxation along other two directions every time.

Fig. 2(e) and (f) explained the reason of the chosen of the structures of path P5. As shown in the upper part of Fig. 2 (f), the orthogonalized unit cell of the ε phase formed in the γ→ε phase transition was selected as the calculation structure. Suppose the γ→ε phase transition was in accordance with the Shoji-Nishiyama (S-N) OR model[9, 90], because the parent phase γ in the γ→ε transition was the productive phase in the α→γ

transition in tension process along the [010] direction of α-Fe single crystal in the [010] direction, it could be built a connection between [111] γ and [010] α, which were the tensile directions of the two phase transition processes. According to the Bain model, the tension **D** along the [010]α direction can be decomposed into a shear component **s** parallel to the (110)α plane along the CD ($[\bar{1}10]\alpha$) direction and a tensile component **n** perpendicular to this plane, as shown in Fig. 2(e). The component **n** always perpendicular to this plane initially identified as (110)α which identification would be changed from (110)α to (111)γ in the $\alpha\rightarrow\gamma$ transition. So, if we use the deformation along the [111] γ direction as **n**, the connection of the two transitions could be created. Denoted the changed structures as α', it could be seen that direction of **n** was actually changed from [110]α to [210]α' in the α→γ transition and **s** always along $[\bar{1}10]\alpha$ or $[\bar{1}10]\alpha'$ in the whole process. This meant that the shear lattice plane in the deformation process was always the same and **n** was always perpendicular to that plane. The ε phase would be formed by shearing along one of the <112>γ directions in γ phase, with the OR being $[111]\gamma//[0001]\varepsilon$, $[11\bar{2}]\gamma//[10\bar{1}0]\varepsilon$, $[1\bar{1}0]\gamma//[1\bar{2}10]\varepsilon$. Suppose such shearing shown in the lower part of the Fig. 2(f) was driven by **s**, the structure used in P5 as shown in the upper part of the Fig. 2(f) was the formed structure in the $\gamma\rightarrow\varepsilon$ transition and (0001)ε//(111) γ//(110)α. If *h* was denoted as the interlayer spacing of the structure in the **n** direction, no matter how **n** was changed, *L* always equals to *2h*. Thus, as seen from Fig. 2(e), *h* satisfies the following relationship:

$$h = \frac{AC \cdot BC}{CD}$$
$$CD = \sqrt{AC^2 + BC^2} \tag{6}$$

So, with P5, the average atomic energy E_{P5} could be calculated by changing lattice length *L* along $[111]\gamma//[0001]\varepsilon$, and relaxed in other two directions. The magnetic state was set to NM in this calculation. The generated set of K points is 7×6×12.

For comparing the changes of energies, the reference state was chosen as the ground state of the FM α-Fe and relationship between the energy and deformation was defined as below:

$$\delta L = \frac{L' - L}{L}$$
$$\Delta E = E_{pn} - E_{ref}, n = 1, 2, 3A, 3F, 4, 5 \tag{7}$$

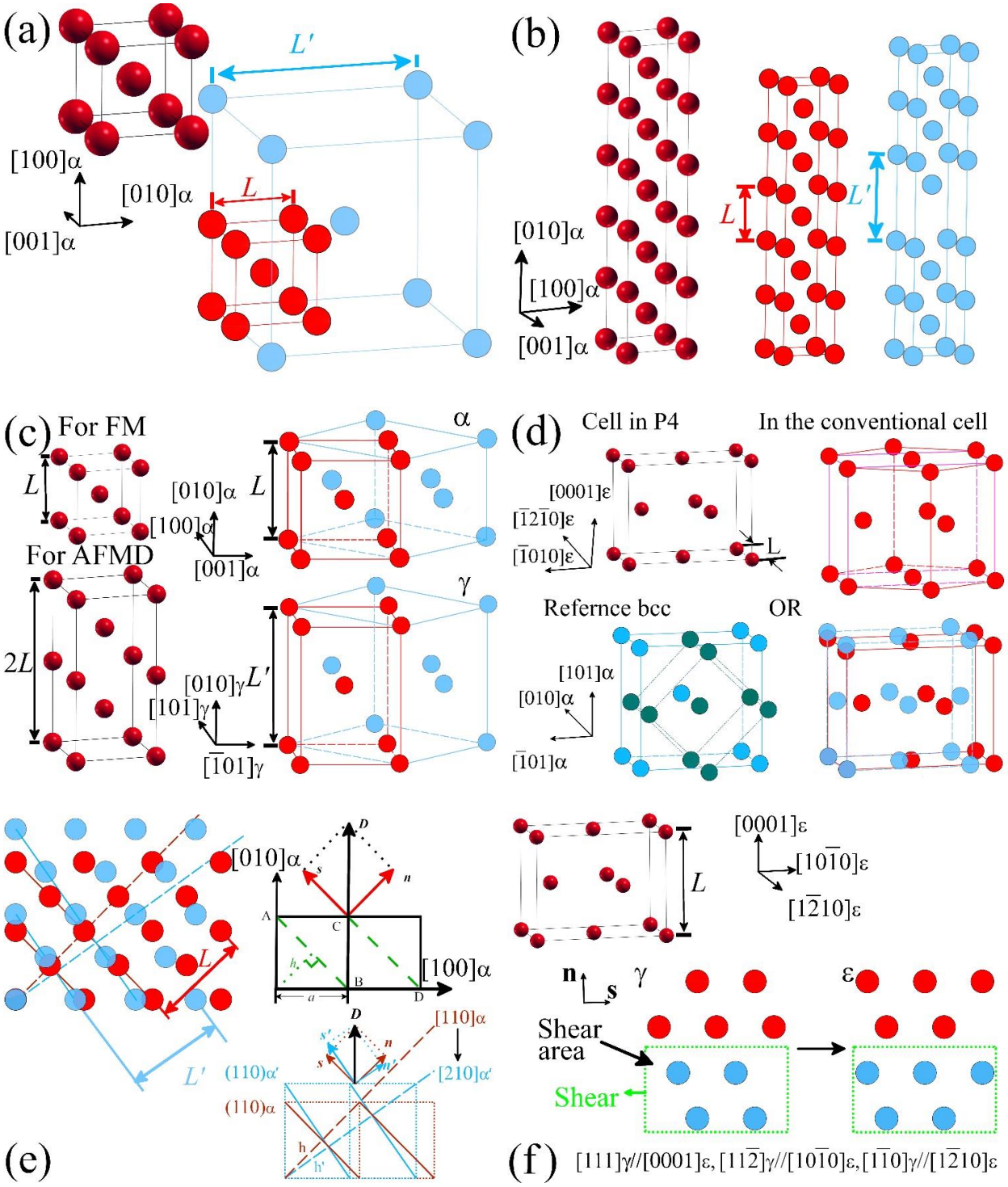

Fig. 2. Modeling for First-principle calculations. (a) unit cell of bcc structure, *L* would be changed to simulate the uniformly expansion. (b) for fracture analysis, a structure stacked by 5 bcc cells. (c) for the α→γ transition, the upper left one was used with FM, the lower left was used with AFMD, the right part has shown the OR of the Bain model. (d) for the calculation of α→ε transition, it's initial state was the orthogonalized cell of ε phase shown in the upper left part, which satisfies the Burgers OR. (e) Decomposition of the tension **D** and the connection of two phase transitions. (f) shearing model for γ→ε transition and the orthogonalized cell of ε phase according to the S-N OR, for the calculation with loading along the [111]γ direction.

3. Results and discussion

3.1 Quasi-cleavage fracture and microscopic plasticity

We proposed an algorithm in our simulations to track the position of the crack tip, and the SIF of the mode I loading was extrapolated to the crack tip at different times. Results in Fig. 3 (a-b) show that the crack length has no obvious change until it begins to grow at the time t_{Ie} = 202 ps with an SIF of 2.672MPa·$m^{1/2}$ at the crack tip. The crack propagation starts to accelerate after the time t_{IC} = 230 ps, denoting the critical SIF (K_{IC}) of 3.354 MPa·$m^{1/2}$ at this moment. When the time is increased from point K = 243 ps to point L = 294.5 ps, the crack is propagated unstably and the associated SIF at the crack tip decreases rapidly. The distance of unstable propagation is 83.4 Å, with the velocity of 161.94m/s. After the unstable propagation, there is a slow propagation stage of the crack, where the SIF is gradually increased to near 0, indicating that the tensile load on the specimen is completely released in the failure process and the change in energy and structures has reached a dynamic equilibrium. It has been reported that the K_{IC} for cleavage fracture of most materials is about 1 MPa·$m^{1/2}$ [97]. Therefore, value of K_{IC} in this work suggests the quasi-cleavage fracture process of α-Fe, which means that the plasticity should be happened. It can be seen from Fig. 3(a) that, during the propagation of the accelerated crack from t_{IC} to K, the crack length continues to expand with oscillation of the crack tip. It implies that the plastic deformation such as volume expansion or disordering arrangement of atoms happens near the crack tip during the crack propagation. Fig. 3(c-e) shows the results of dislocation analysis using ovito's DXA algorithm, which can effectively identify various types of dislocations [98, 99]. Combined with the dislocation emission shown in Fig. 3 (c,d), it can be seen that the crack initiated the first dislocation at t_{Ie}, with the Burgers vector of [010], meaning that the corresponded SIF should be the critical SIF K_{Ie} for dislocation emission [100–103]. However, no dislocation emission has been observed during the crack propagation in a later period of time, including the crack acceleration and unstable propagation stages. However, dislocation emission is observed again once the crack starts to propagate smoothly at the time of L, in which the Burgers vector of dislocation at the front of the crack was also [010], as showed in Fig. 3(e).

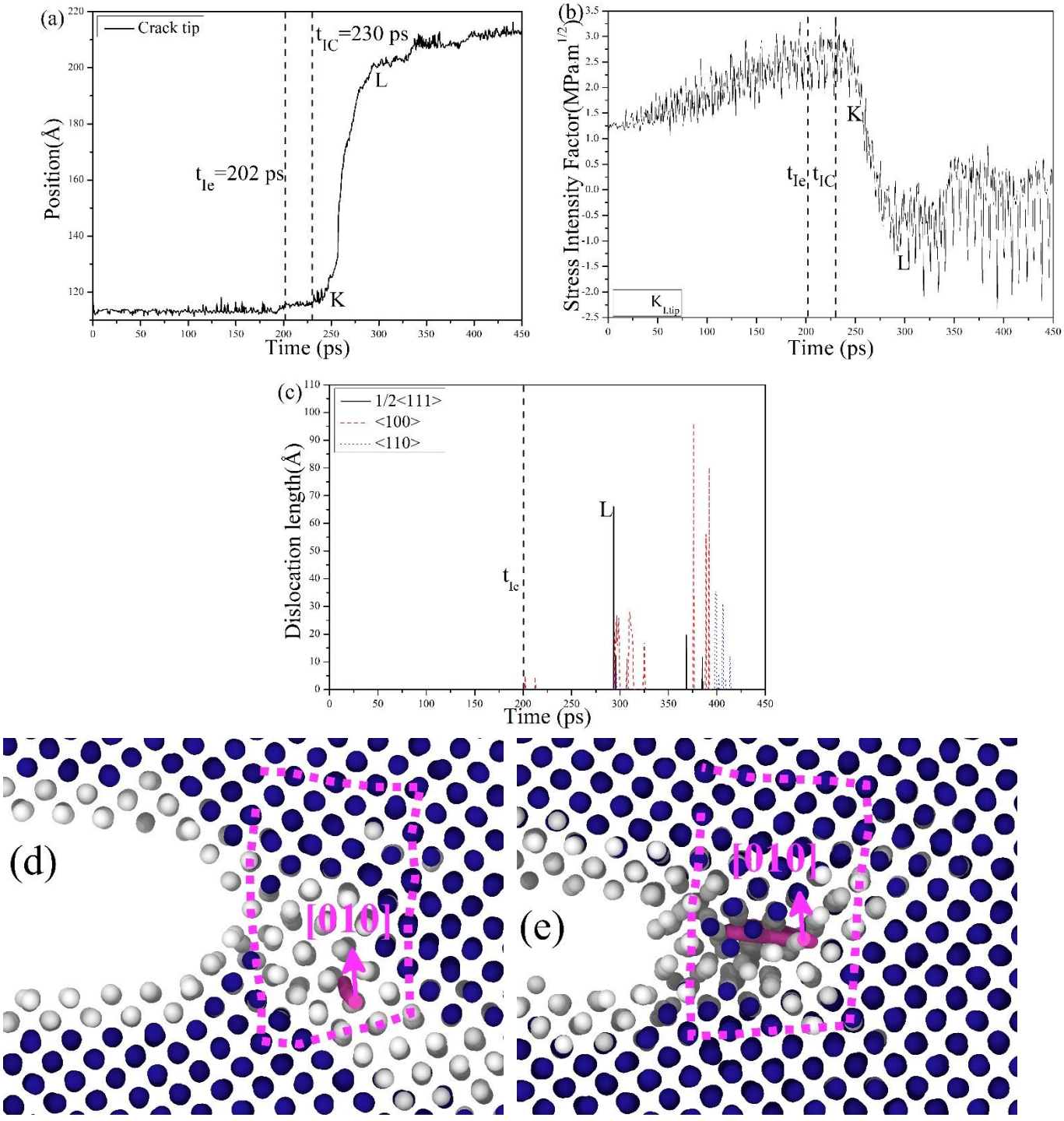

Fig. 3. Crack tip and dislocation emission. (a) The position of the crack tip along the [100]α direction changed with time. (b) The SIF at the crack tip, obtained by an extrapolation method. (c) Length of dislocations and dislocation type near the crack tip at different times. (d) The [010] dislocation near the crack tip, the first dislocation emitted at 202ps; pink arrow points to the direction of the Burgers vector. (e)The dislocation near the crack tip emitted at 294.5ps, pink arrow points to the direction of the Burgers vector.

The results in Fig. 3 indicates that the specimen under tensile loading presents the characteristics of cleavage fracture. However, it is influenced by microscopic plasticity factors, and the plasticity phenomenon is not only caused by the emission and motion of dislocations. It is well known that the cleavage surface of α iron is on

the {100} planes, and its cleavage direction is mainly between <100> to <110> [97, 104, 105]. It has been found that steel is easier to have the cleavage fracture under relatively high loading rate [106]. The loading rates in experiments are commonly about $10^{-3}s^{-1}$ [107, 108], much lower than 10^{8}~$10^{11}s^{-1}$ in MD simulations [107, 109]. We used the loading rate of $3.1\times10^{8}s^{-1}$ in our simulation, which could also result in the obvious characteristics of cleavage fracture along the (010)[100]α direction. However, the oscillation of the crack tip was found during the deformation beyond the KL range. In addition, the duration of this oscillation exceeds the period of 15 ps that the specimen was held after each elongation, reflecting that the plastic deformation might be existed in the process, rather than the cause of high loading rate. In general, the plastic deformation process in crystals is mainly attributed to dislocation slip [110, 111], which is related to the mechanisms of dislocation initiation and migration, and also often observed by electron microscope in industrial pure iron [112]. However, very few dislocations have been seen in our simulation until the crack reaches the slow propagation stage. In addition, dislocations emitted near the crack tip throughout the process are mostly <100> dislocations. According to Cottrell's theory [113], the <100> dislocation on the (010)α plane should be composed of two 1/2 <111> dislocations. Because (010)α plane is not a dense plane, <100> dislocations cannot move easily. Therefore, this type of dislocation can only reduce the crack propagation resistance and thus promote the crack nucleation, but has no contribution to plasticity. As can be seen from Fig. 3(c), the 1/2 <111> dislocation has not been found before the crack propagation during the loading process. It may be caused by the condition of high-speed loading, which can lead to the high magnitude of tension stress that favors the generation of <100> dislocations. Dislocation emission is completely suppressed in the stages of crack acceleration and instability expansion until the moment at L when 1/2 <111> dislocations starts but quickly disappears. Moreover, the calculated K_{IC} and K_{Ie} in our work are listed and compared with other reported data in Table 1, where FEAt stands for finite element combined atomic scale calculation, and MS stands for molecular statics method. As shown in Table 1, our K_{IC} is close to others, especially to the α-Fe single crystal experimentally measured by Hribernik at 77K, hence validating our calculation method in this work. The difference between our results and others' might be not caused by different interatomic potentials.

Table 1 SIF of α-Fe single crystal

	SIF ($MPa\cdot m^{1/2}$)	Temperature (K)	Dislocation Type	Crack Orientation	Method
K_{Ie} (Current work)	2.672	300	<100>	(010)[100]	MD

K_{IC} (Current work)	3.354[1]	300	-	(010)[100]	
	4.521[2]	300	-	(010)[100]	
K_{IC} [105]	2.5~6.4	77	-	(100)[010]	Static-Dynamic
	14.8	298	-	(100)[010]	Test
	4.1~6.0	77	-	(100)[011]	
	16.1	298	-	(100)[011]	
K_{IC} [48]	1.19~1.31	-	-	(100)[010]	FEAt
	0.76~1.07	-	-	(100)[011]	
K_{Ie} [101]	0.96	300	1/6<111>	(010)[10$\bar{1}$]	MD
K_{IC} [101]	1.80	300	-	(010)[10$\bar{1}$]	
K_{IC} [114]	0.98~1.39	-	-	(100)[001]	MS
	0.92~1.21	-	-	(100)[011]	
K_{Ie} [114]	1.31~1.63	-	1/2<111>	(100)[001]	
	1.62~2.00	-	1/2<111>	(100)[011]	
K_{Ie} [115]	0.96	300	1/2<111>	(111)[11$\bar{2}$]	MD
K_{IC} [115]	0.93	300	-	(111)[1$\bar{1}$0]	

1. This K_{IC} is obtained under the loading rate $3.1\times10^{8}s^{-1}$.

2. This K_{IC} is obtained under the loading rate $1.55\times10^{8}s^{-1}$.

. (是否可以简化或者删除这段讨论？)

3.2 Strain-induced martensitic transformations under tensile loading

Snapshots are taken at different times with identified structures by implementing the ACNA algorithm [57] during the tensile loading. As shown in Fig. 4, the α, γ, and ε phases of iron have been represented by the blue, green, and red colors, respectively. Fig. 4(b) shows that the arrangement of a small set of iron atoms in front of the crack tip become disordering at 202 ps, and γ phase starts to nucleate near there too, which would increase the local plasticity. Since 220 ps, the crack blunting is occurred with the increasing of the number of disordered atoms near the crack tip, as shown in Fig. 4 (c). After that, the nucleation, growth, and disappearance of γ phase is continuously produced near the crack tip during the whole loading process. Specifically, the nucleation of ε phase from inside of γ phase has also been observed in this process. From fig.

4 (d) and fig. 4 (f), it can be seen that the crack begins to propagate rapidly along the (010)[100] direction of α-Fe from 230ps to 294.5 ps. With rapid propagation of the crack, γ phase is symmetrical distributed on both sides of the fracture surface near the crack tip. Fig. 4(e) shows that a void is nucleated in front of the crack tip and grown towards the crack tip. During this process, the crack is propagated steadily, and the fracture morphology became rough, indicating the ductile fracture characteristics [119]. Part of the γ phase formed near the crack tip could move a short distance when the crack is propagated steadily, and the ε phase might be nucleated. At the later stage of tensile loading process, more ε phase could be observed inside of the γ phase, as shown in Fig. 4(i). Therefore, ε phase is nucleated from the pre-formed γ phase and there is no ε phase directly formed in the α phase during tension, indicating that the polymorphic transformation follows the path α→γ→ε in our work.

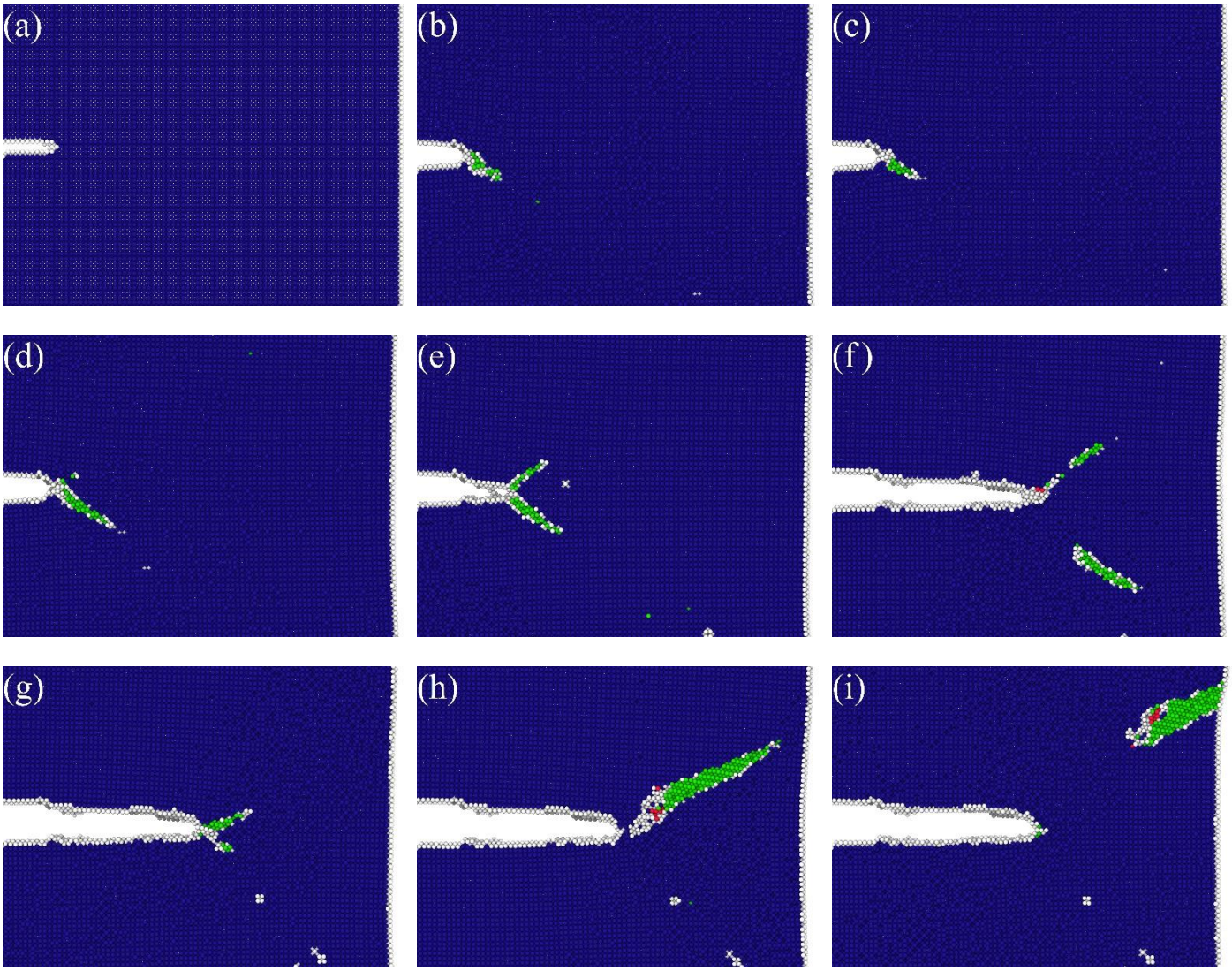

Fig. 4. Crack propagation in the specimen under tension along [010] direction. (a) 0 ps, start of simulation. (b) 202ps, crack blunting, amorphization occur near the crack tip, γ phase nucleation. (c) 220ps, amorphization effect enhanced, γ phase starts to grow (d) 230ps, rapid propagation of the crack. (e) 256.5ps, rapid propagation of the crack, with a void formed in front,

reveals the features of fracture with growth and coalescence of micro-voids. (f) 294.5ps, steady extension of the crack starts, part of γ phase move away. (g) 326ps, steady extension of the crack, disappear and nucleation again of γ phase. (h) 335ps, γ phase move away from the crack tip, and formation of ε phase inside γ phase. (i) 343ps, stable ε phase.

The localized coordinating polyhedron is analyzed for identifying the details of the disordered zone at the crack tip, where 4 kinds of characteristic polyhedral cluster structures in liquid and amorphous are observed. As shown in Fig. 5, their voronoi indices are: <0,4,4,0>,<0,3,6,0>,<0,2,8,0> and <0,2,8,1>, where $<n_3,n_4,n_5,n_6>$ represents respectively the number of <triangle, quadrilateral, pentagonal, hexagonal surfaces> in a coordinating polyhedron. The existence of these cluster structures shows that the amorphization effect [122] occurs during tensile loading with high strain rate. Because of the flow plasticity in amorphous, the disordered structure near the crack tip will promote the occurrence of DIMTs [123].

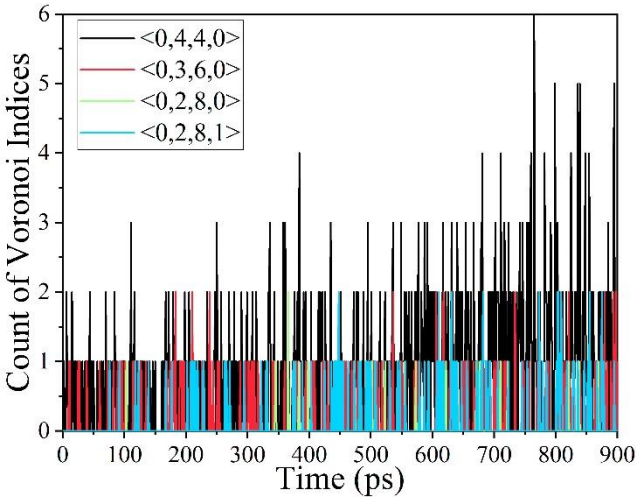

Fig. 5. Amorphous cluster structures in front of the crack tip, 4 kinds of characteristic polyhedral for cluster structures in liquid and amorphous have been observed, which indicates the occurrence of the amorphization effect.

The occurrence of phase transformation during the tensile loading process was also modeled by the first-principle theory. The lattice constants and magnetic state of phases of α-Fe are listed in Table 2. Fig. 6 (a) and (b) give the ΔE-V and ΔE-δL relationship plots, respectively. The results show that the energy along the P1 path is the highest except near the equilibrium state, which indicates that the standard structure of α-Fe must be broken during tensile loading. The energy for structural evolution along path P4 is lower than along P1 but higher than others, which suggests that α→ε phase change may not be occur. Consistently, Fig. 6(c) shows that ε cells will be transformed to the bcc structure and then non-magnetic fcc along this path under tension, resulting in a higher energy state. Notably, energy of two curves for the α→γ phase transformation with Bain model along P3 path, as shown in Fig. 6(b), are basically lower than that along the P2 path. It is slightly higher than that along the P2 path, only after the occurrence of γ phase with the axial strain exceeding 113%. This indicates that the α→γ phase transformation is possible in the α-Fe single crystal with a (010)[100] pre-crack

of mode I fracture under tension along the [010] direction. Note that the energy along path P3 with the AFMD magnetic state is slightly higher than that with the FM magnetic state, indicating that the magnetic state of pure α-Fe stable structure is FM. As for the P5 path, it is found that the corresponding energy is higher than that of P3 path before the formation of γ phase, but is lower once the γ phase is formed with the axial strain reaching 50%~60%. This result shows that ε phase is initiated from the pre-formed γ phase under the tensile loading. With increasing of shearing during further plastic deformation [129], γ→ε transition has been promoted by the slip on the close-packed planes of γ phase. After forming ε phase, as shown in Fig. 6(b), energy change along P5 path tends to be flatten. The MD simulations results and the energy curves obtained from the first-principle calculations indicate that the α→γ and γ→ε phase transformations are possible in the simulated system during mode I fracture process under tension. The ε phase can be completely transformed from the γ phase, both of which are formed before the start of cleavage fracture.

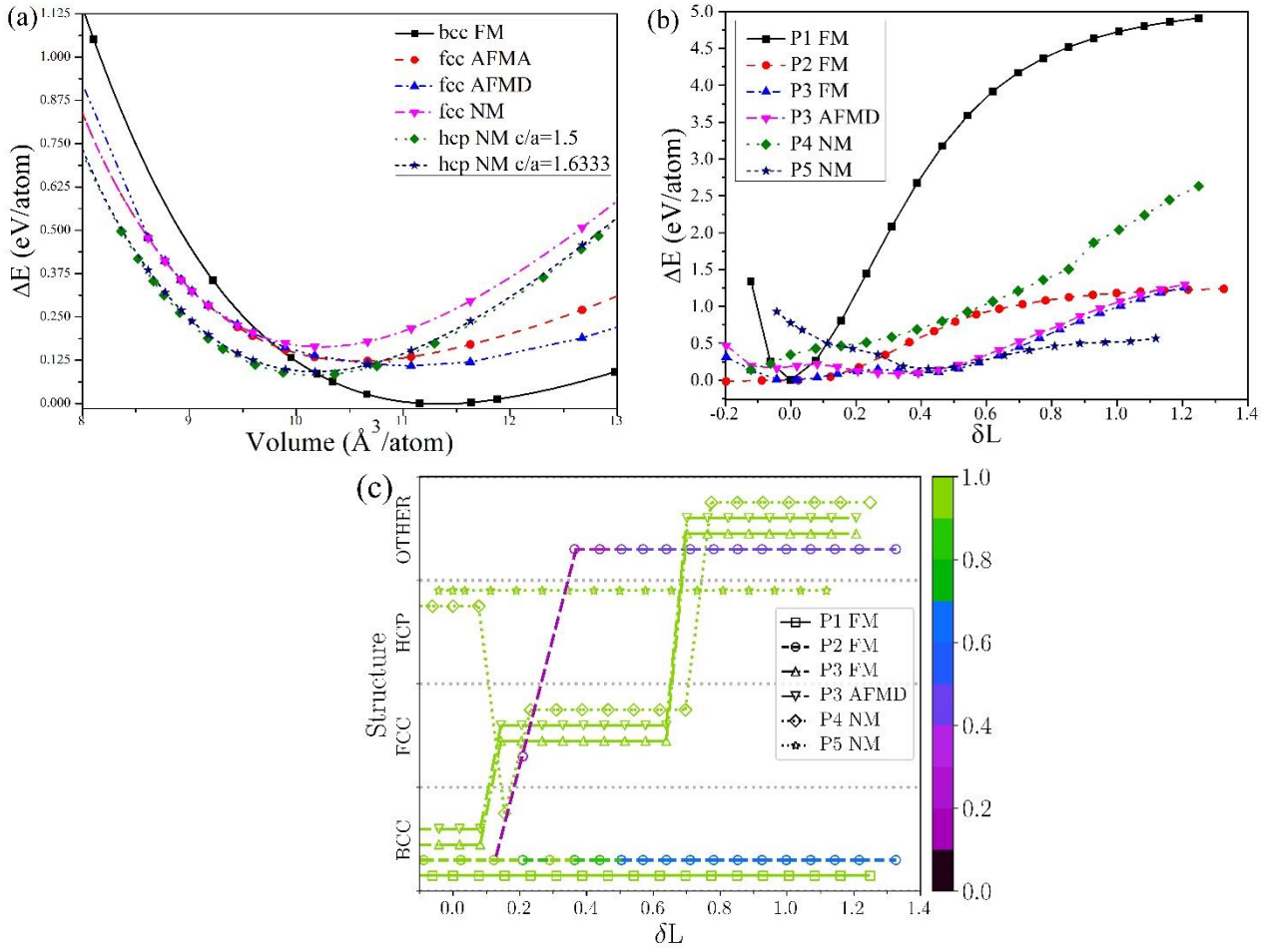

Fig. 6. Phase transformation and crack growth during tension. (a) ΔE-V relation. (b) ΔE-δL relations, δL is the axial relative change of the study region under different structural evolution paths. (c) structural changes, the ACNA algorithm is applied to identify structures in the process of loading.

Table 2 Lattice constants and magnetic states for pure iron

Phase	a(Å)	c/a	Magnetic states
α	2.845	1	FM
γ	3.537	1	AFMD
ε	2.465	1.5	NM

Fig. 7(a) shows the counts of the product γ and ε phases during the tensile process. Combing the results in Fig. 3(b) and Fig. 7(a), it is found that count of γ phase keeps increasing with certain fluctuations until the SIF at the crack tip reaches K_{IC}. After that, the growth rate of γ phase is obviously slowed down once the crack propagation became rapid and unstable. This might because the inverse martensitic phase transformation α→γ is an endothermic reaction [131]. SIF decreases rapidly after t_{IC}, and γ phase still increases for a while. When t = 350ps, both SIF and count of γ phase are decreased to their minimum values, while count of ε phase become maximum. This indicates that α→γ transition might cause the stress relaxation in the specimen and the transformation γ →ε during the further tension.

Therefore, Fig. 7 (b-e) gives the atomic structures of γ and ε phases, and the ORs between them. Specifically, stacking faults is occurred under further tension, leading to the layered ε phase insides of γ, as the inset of zone III shown in Fig. 7(b). In order to confirm the occurrence of phase transformation, we used the SAED method [63, 64] in the present work to determine the ORs between three phases in the phase-transformation region identified by the ACNA algorithm. The zone I in Fig. 7(b), which contains the atoms with positions located as 295Å>x>275Å, 230Å>y>188Å, 34.3968Å>z>0Å, was taken to determine the SAED pattern, as shown in Fig. 7(c,d), where the OR between α phase and γ phase is [001]α//[011]γ and $(1\bar{1}0)\alpha//(\bar{1}\bar{1}1)\gamma$, obeying the Nishiyama-Wassermann (N-W) relation [90, 130]. Besides, ε phase occurred in γ phase denotes that OR as: (111)γ//(0001)ε and $[1\bar{1}0]\gamma//[1\bar{2}10]\varepsilon$, which satisfies the S-N OR [90]. Notably, the layered ε phase distributes along the $[11\bar{2}]$ γ direction on (111)γ plane, in accordance with the mechanism for γ→ε nucleation proposed by Olson and Cohen [9], and the HRTEM observed OR in AISI 304 austenite stainless steel by Yang and Zhang[13, 14]. Moreover, the atomic model responsible for the ORs among these three phases are plotted in Fig. 7(e), in which the interface of the α-γ phases $(\bar{1}\bar{1}1)\gamma$ is perpendicular to the interface of the γ-ε phases (111)γ.

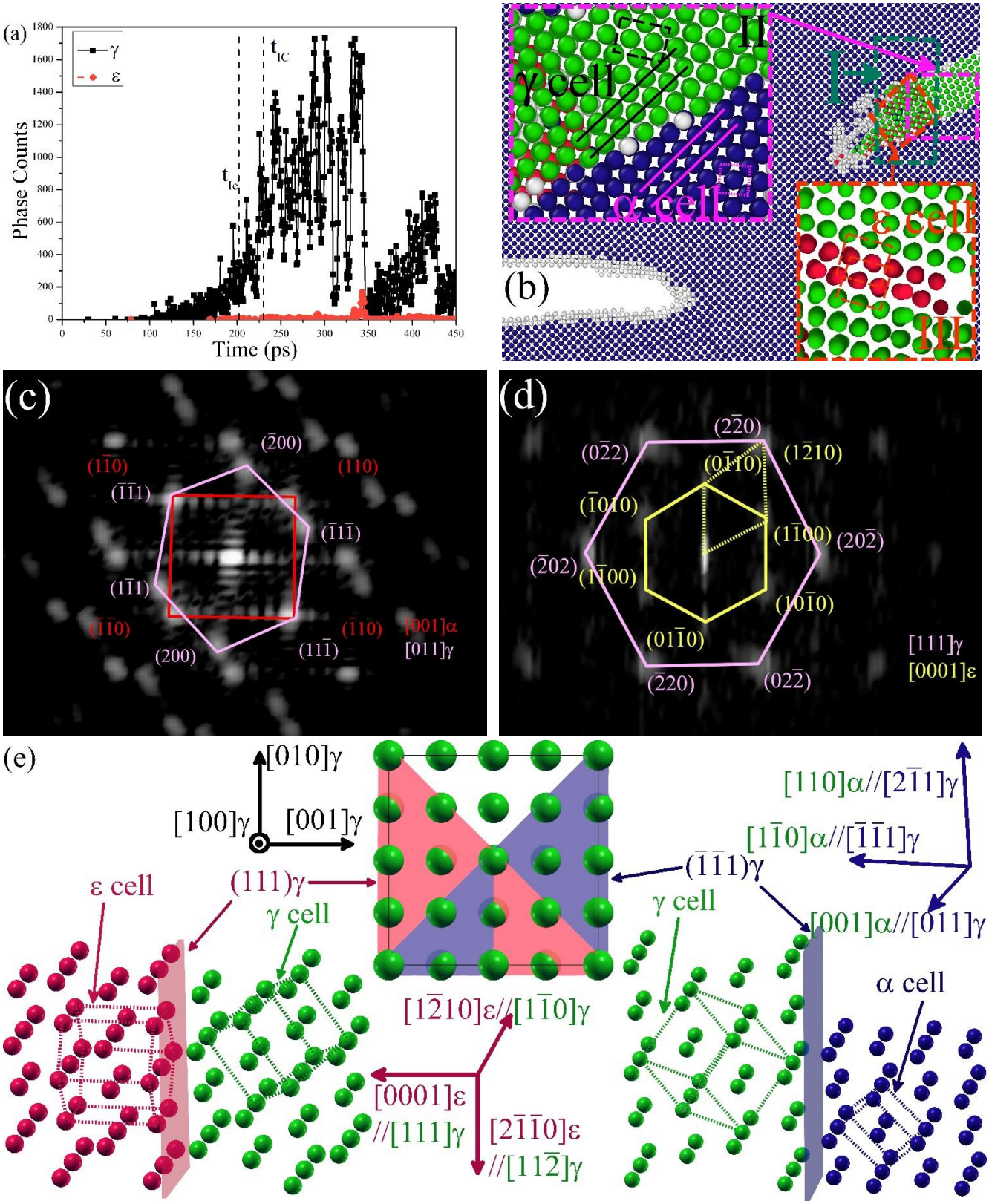

Fig. 7. Strain-induced γ phase and ε phase. (a) Counts of atoms belong to γ phase or ε phase. (b) Stabler ε phase forms at 342.5ps, there are both γ phase and a relatively large number of atoms of ε phase. (c) Diffraction patterns with virtual SAED method along [001]α direction at 342.5ps. (d) Diffraction patterns with virtual SAED method along the [111]γ direction at 342.5ps. Atoms belong to α phase have been removed to enhance imaging for the concentration of ε phase being too small.

(e) ORs among three phases. In the middle was the γ phase with two interfaces with the α and the ε phases.

We also discuss the geometrical relationship between growth direction of γ phase and the (010)[100]α tension direction. As shown in Fig. 8(a), the angle ξ between the growth direction of γ phase and (010)[100]α direction keeps about 36° during most of the time. It could be increased to about 50° with rapid propagation of the crack once the serious deformation of the specimen makes the crack unstable. The slip deformation of α-Fe can be activated in three kinds of slip systems, such as {112} <111>, {110} <111> and {123} <111> [128, 132–134], or along the direction of the max shear stress [135, 136], or along <110> or <001> direction [132]. {112} <111> and {110} <111> are preferential slip systems in α-Fe at relative low temperatures [132]. The intersection between {112} and (001) planes with a crystal orientation of $[2\bar{1}0]$ denotes the angle ξ of 26°. While the intersection between {110} and (001) planes with a crystal orientation of $[10\bar{1}]$ induces the angle ξ of 45°. Note that the value of the angle ξ in the present work is 36° between the above two angles, as shown in Fig.8(c). Therefore, we believe that the γ phase is formed by the shear that comes from the competition between two slip systems-, such as the cross-slip. For example, as shown in Fig. 8(b), the same slip $[\bar{1}1\bar{1}]$ direction is located at the (121)$[\bar{1}1\bar{1}]$ system and the (110)$[\bar{1}1\bar{1}]$ system. Such two slip systems are all related to the transition of α→γ, as reported by Ou et al. [137]. So, atoms would slip both on (121) and (110) planes if load is applied. If the strain rate was high enough, shear actions could be activated in the triangular green-color region, resulting in the phase transformation in this region. At the same time, the resistance of phase transition would be reduced, as a result of the size effect of small volume and amorphization near the crack tip [122]. Finally, a triangular zone with the γ phase would be formed near the crack tip, as shown in Fig. 8(b), which is projected to (001) plane of the geometrical structure of atoms in the continuous formed γ phase, as the deformation process shown in Fig. 4. According to Bowles-MacKenzie (BM) model [21, 32, 87, 107], as shown in Fig. 8(b), γ phase can be formed with two kinds of shears in (121)[111] and (110)[111] slip systems: (1) shearing along the $[\bar{1}1\bar{1}]$α direction on the (121)α plane; (2) shearing along the $[\bar{1}1\bar{1}]$α direction on the (110)α plane. By using the lattice constants listed in Table 2, the possible ORs between α and γ phases are obtained and listed in Table3, in which the orientation differences less than 1° are ignored. It can be seen that OR between α and γ phases, which is consistent with our simulation, can be obtained by slipping along $[\bar{1}1$ $\bar{1}]$α direction on the (121)α plane. Fig. 8(d-f) shows the structure of the specimen near the crack tip at 228.5ps in different view angles, where phases are identified by using the ACNA algorithm. At this moment, γ phase

is obviously observed with a shear about 13° along the $[1\bar{1}0]\alpha//[1\bar{2}\bar{1}]\gamma$ direction on the $(110)\alpha//(11\bar{1})\gamma$ plane, as marked with ω in Fig. 8(d). This shear might be came from the slip in $(110)[\bar{1}1\bar{1}]\alpha$ system, in which a slip along $[\bar{1}1\bar{1}]\alpha$ direction can be decomposed into two $[1\bar{1}0]\alpha$ and $[001]\alpha$ directions. As shown in Fig. 8(e,f), there is a shear about 10° along the $[\bar{1}1\bar{1}]\alpha//[\bar{1}10]\gamma$ direction on the $(121)\alpha//(110)\gamma$ plane (marked as θ in the figure), which is came from the slip in $(121)[\bar{1}1\bar{1}]\alpha$ system. Twinning-like structures have been formed between $(101)\alpha$ and $(0\bar{1}0)\alpha$ planes by the activation of $(121)[\bar{1}1\bar{1}]\alpha$ system, which makes the dilatation along the $[010]\alpha$ direction and rotates the $(101)\alpha$ with the axis of $[10\bar{1}]\alpha$.

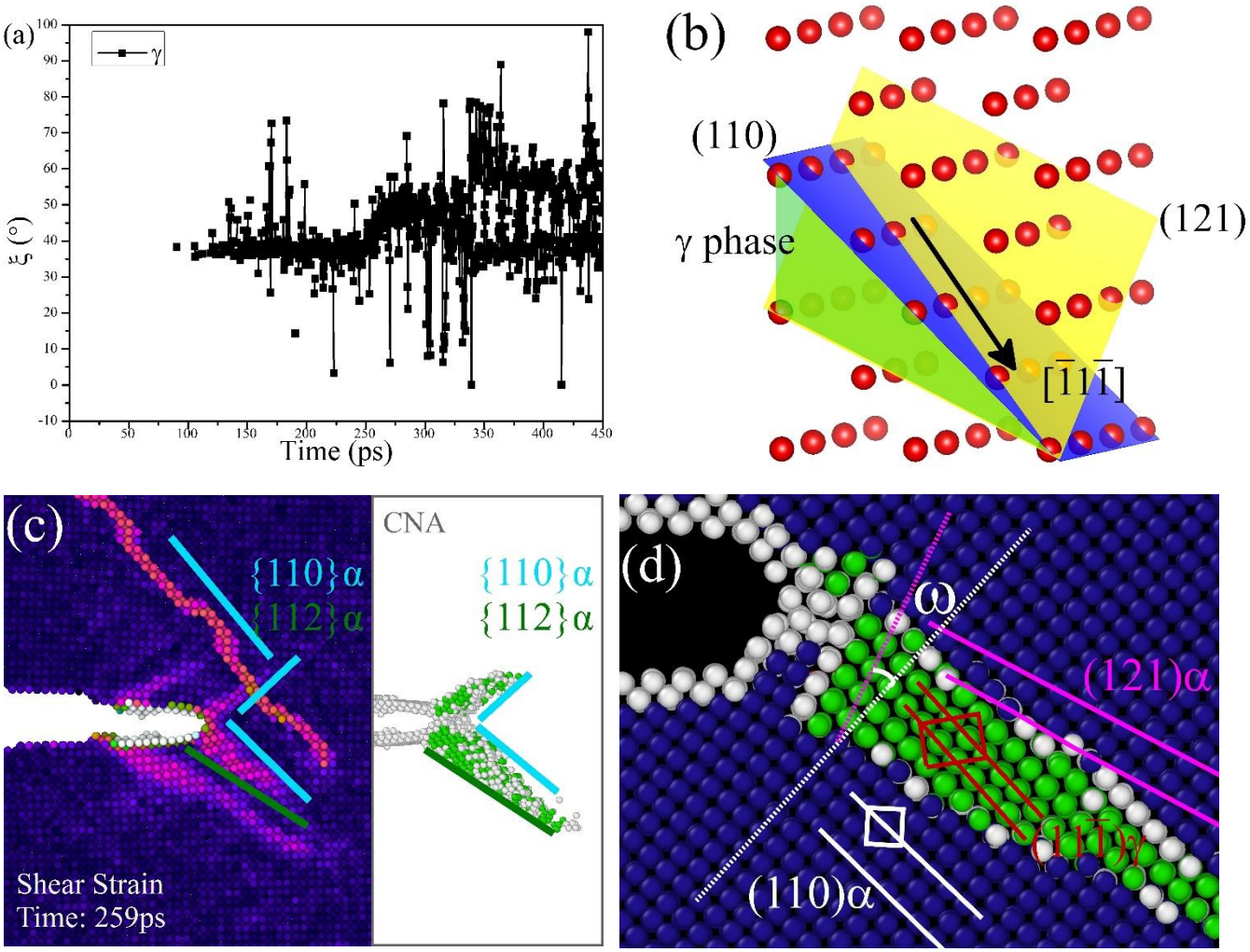

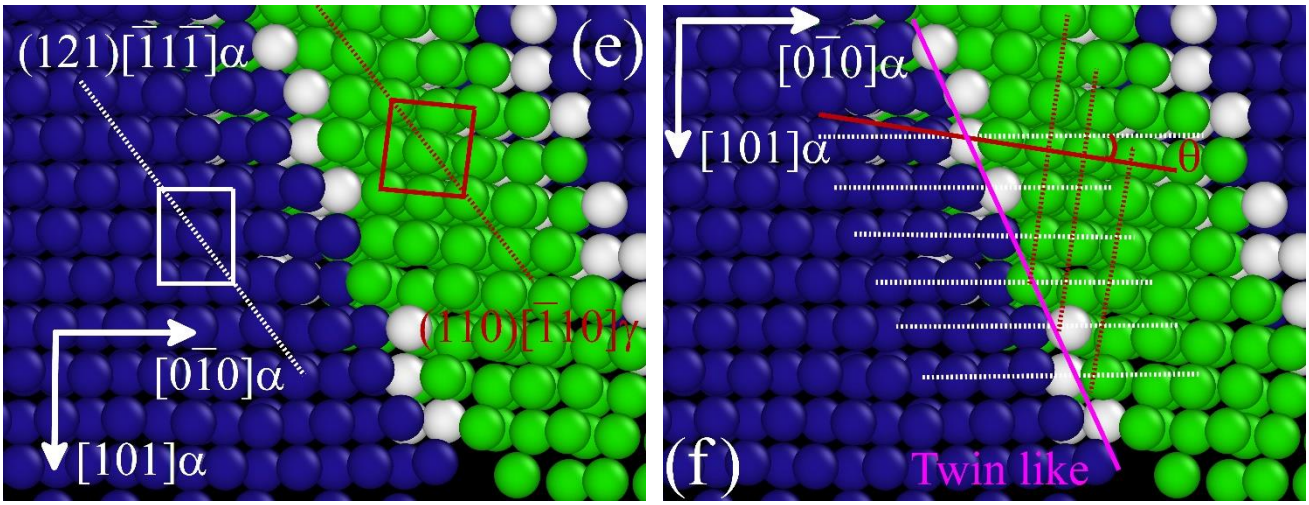

Fig. 8. Formation of γ phase. (a) angle ξ, between growth direction of γ phase and (010)[100]α, keeps about 36° most of the time. (b) (121)[$\bar{1}1\bar{1}$] and (110)[$\bar{1}1\bar{1}$] slip systems in front of the crack tip, these two systems have a same slip direction [$\bar{1}1\bar{1}$]. With their competition, α→γ transformation will occur at green colored region by the shear coming from the cross-slip of the two slip systems under large deformation (c) shear strain and γ phase near the crack tip at 259ps. Planes with larger shear have been marked with color lines (d) OR between α phase and γ phase at 228.5ps, which is in accordance with N-W relationship, ω=13°. (e) Another view angle shown the OR. (f) The twin like structures after sharing. θ=10°.

OR between the α phase and γ phase accorded with one of the ORs solved with the BM model, with the assumption that the activated slip system was (121)[$\bar{1}1\bar{1}$]. But it was different when the slip system was assumed to be (110)[$\bar{1}1\bar{1}$]. This may be due to the fact that the phase transition in our simulation is caused by two sets of shears.

Table 3 Martensitic transformation ORs

Shear direction	OR	Type
(121)[$\bar{1}1\bar{1}$]	(011)α//(111)γ, [1$\bar{1}$1]α at the angle of 4.06° to [1$\bar{1}$0]γ	K-S
	(110)α//(1$\bar{1}$1)γ, [1$\bar{1}$0]α at the angle of 1.25° to [12$\bar{1}$]γ	N-W
(110)[$\bar{1}1\bar{1}$]	(011)α//(111)γ,	K-S

	$[1\bar{1}1]\alpha$ at the angle of 1.49° to $[1\bar{1}0]\gamma$	
	$(110)\alpha//(1\bar{1}1)\gamma$,	K-S
	$[1\bar{1}1]\alpha//[1\bar{1}0]\gamma$	

(是否考虑删减这段讨论？)

3.3 Thermodynamic formation mechanisms of γ and ε phases

Fig. 9 gives the tension stress distribution near the crack tip zone with the formation of γ phase in our simulation. It can be seen in Fig. 9(a) that tension stress along the growth direction of γ phase is decreased significantly, and stress concentration is occurred near the crack tip at the beginning of crack propagation, which is higher than that in the process of rapid crack propagation, as shown in Fig. 9(b). It could be seen from Fig. 7(a) that the increase of γ phase slows down during rapid propagation of the crack, while the unstable crack extension is helpful to the formation of new γ phase as shown in Fig. 9(b).

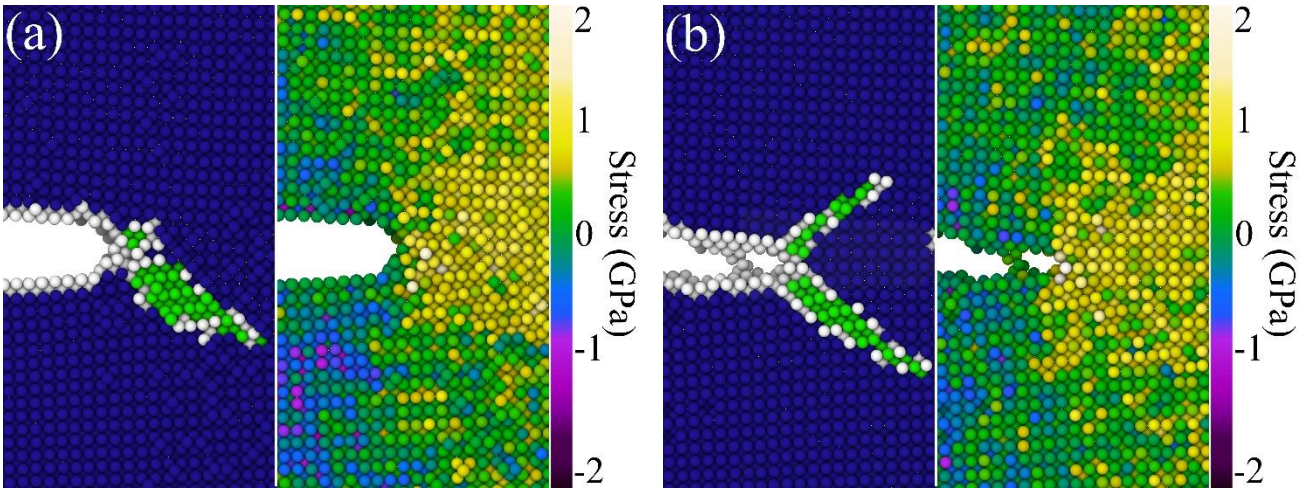

Fig. 9. Phase transformation and stress distribution near the crack tip. (a) Crack blunting at 213.5ps. γ phase forms at the cross region with tension stress between the two slip systems. (b) Rapid propagation of the crack at 256.5ps. γ phase occurs at the cracking surface.

On one hand, it has been pointed out that the shear effect in tensile stress is more helpful to the nucleation of martensite than that in compressive stress [129]. On the other hand, volume change and the orientation of the newly formed phase during the marentisitc transformation could result in the TRIP effect [141], which play important roles in the further strain-induced martensitic transformation [142, 143]. In other words, the mechanical driving force for the strain-induced martensite nucleation ΔG_{mech} is believed as the summation of contributions from the volume change and shear stress [1, 2, 8, 144]. Therefore, the volume change and the

mismatch of the two phases are not only the source of the increasing of plasticity, but also the important factors for inducing phase transformation in the deformation process.

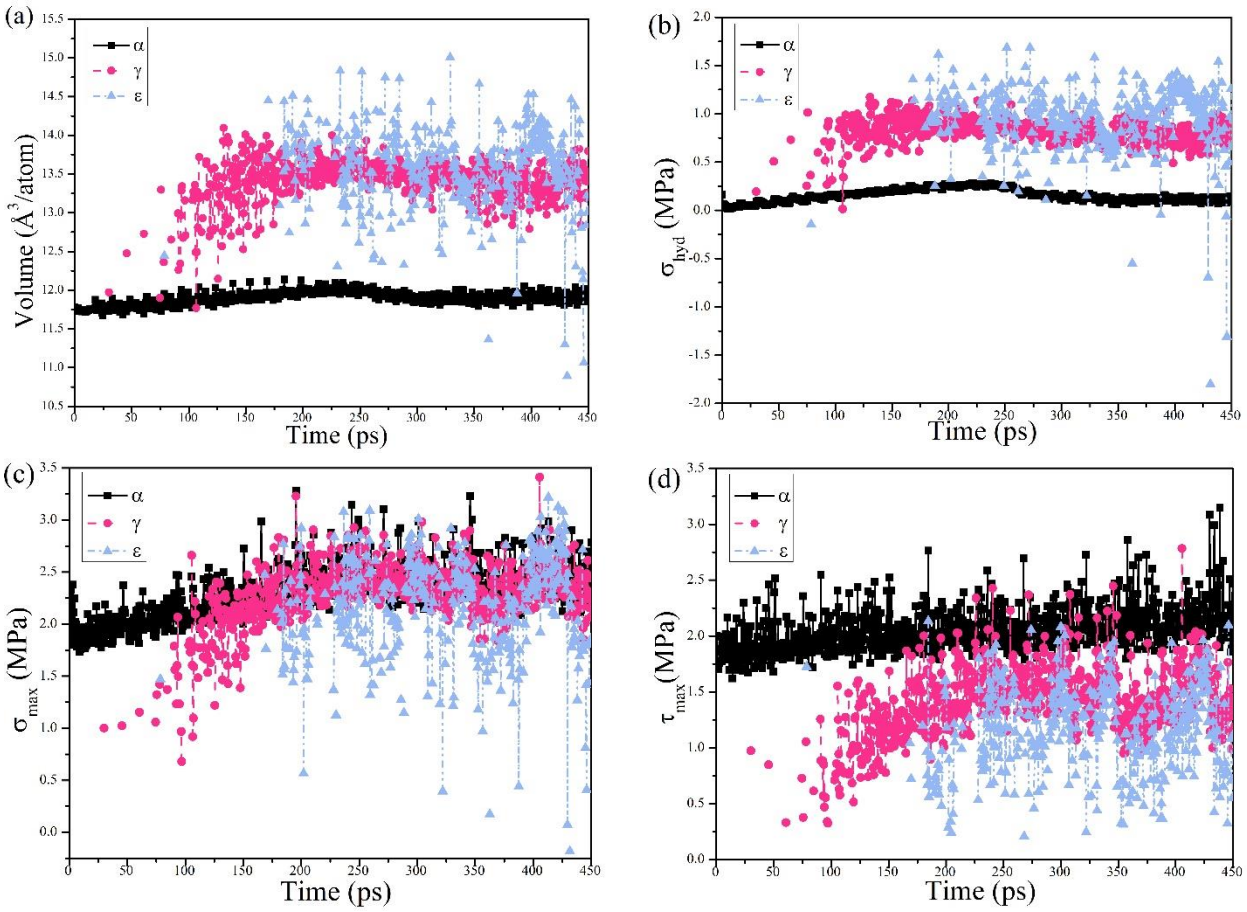

Fig. 10. Stress and average volume analysis of α, γ and ε phases. (a) average volume of atoms, averaged volume of atoms in the production phases increases rapidly with deformation and their equivalent volumes are obviously larger than that of the α phase. (b) hydrostatic stress of atoms, hydrostatic stress in the production phases is also larger than that in the α phase. (c) maximum principal stress of atoms, maximum principal stresses in the γ and the ε phases are lower than that in their matrix phases at the beginning of phase transformations, which indicates that the stress state in matrix phases will be relaxed by such transitions but fracture must happen at last due to the maximum principal stress rapid reaching the level in the matrix phases. (d) Maximum shear stress of atoms, the maximum shear stress in the γ and the ε phases keeps lower than in their matrix phases within the whole deformation process, this means that γ and ε phases form all the time.

Fig. 10(a) shows the averaged atomic volumes V_α, V_γ, and V_ε of the α, γ, and ε phases, respectively, with the increase of loading to equilibrium. It can be seen that V_α is increased slightly before the crack propagates became unstable before 210 ps indicating that there is no obvious damage in the specimen. While, there is an obvious decrease of V_α once the rapid propagation of the crack from 210ps to 230ps. On the other hand, the V_γ of the γ phase and V_ε of ε phase are significantly increased from ~100 ps and 210 ps, respectively, after which the atomic volumes of these two phases are almost the same and keep unchanged onwards. It also indicates that that the ε phase is nucleated from pre-formed γ phase, rather than directly from α phase during tension, leading to the α→γ→ε transformation. In addition, Fig. 10(b) shows the corresponding the hydrostatic stress versus time during the tension process, indicating that the two newly transformed γ and ε phases possess higher energy states that matrix α phase although the α→γ→ε phase transformation is induced during the tension. This mainly because these two newly transformed phases are formed in the stress concentration areas.

Fig. 10(c-d) gives the maximum principal stresses and maximum shear stresses versus times during the tension, respectively. It could be observed that stresses relaxation not only occurs in α→γ transition near the crack tip, but also in γ→ε transition inside the γ phase. With lowering the maximum principal stress and maximum shear stress in the product phases, plasticity would be increased with the delay of the crack propagation. But the maximum principal stress in both phases continue to rise and quickly catch up that in α phase, which would weaken the stress relaxation effect. Shear stress is commonly believed as the main reason for the strain-induced martensitic transformation. With the increasing of deformation, it could be seen from Fig. 10(d) that the corresponding increased maximum shear stresses in the γ and ε phases are both always lower than that in α phase, where these stresses in the ε phase is lower than in the γ phase, indicating that the phase transformations would continue.

The mechanical component of the driving force ΔG_{mech} for the strain-induced martensitic transformation in perfect single crystal satisfies the relationship below [1]:

$$\begin{aligned} \Delta G_{mech} &= \sigma : \varepsilon \\ \Delta G_{chem} + \Delta G_{mech} &= 0 \end{aligned} \tag{8}$$

Volume and shear influence this transformation. The upper limit of ΔG_{mech} can be estimated using Eq.(8) with the replacement of the maximum principal stress σ_{max} and the maximum shear stress τ_{max} by the principal stress σ and shear stress τ, respectively. The volumetric strain δ and the shear strain invariant γ can be obtained by implementing the Shimizu method [58].

$$\Delta G_{mech} = \sigma_{max}\delta + \tau_{max}\gamma \tag{9}$$

In Eq.(8), $\sigma_{max}\delta$ reflects the influence of the principal stress and volumetric strain, while $\tau_{max}\gamma$ reflects the influence of the shear stress and shear strain. These two components can be used to estimate the influence of dilation and shear on the phase transformation, respectively. For short, we denote them as $\sigma\delta$ and $\tau\gamma$. Considering that mechanical part of free energy is not zero in the matrix phase when the phase transformation occurs under tensile loading, these two terms in Eq.(8) need to be modified as:

$$\begin{aligned} \sigma\delta &= \sigma_p\delta_p - \sigma_o\delta_o \\ \tau\gamma &= \tau_p\gamma_p - \tau_o\gamma_o \end{aligned} \tag{10}$$

where the product phase is marked as *p* and the matrix phase is marked as *o*. The maximum effect of volume change and shear on phase transformation during tensile loading can be estimated from Eq.(9).

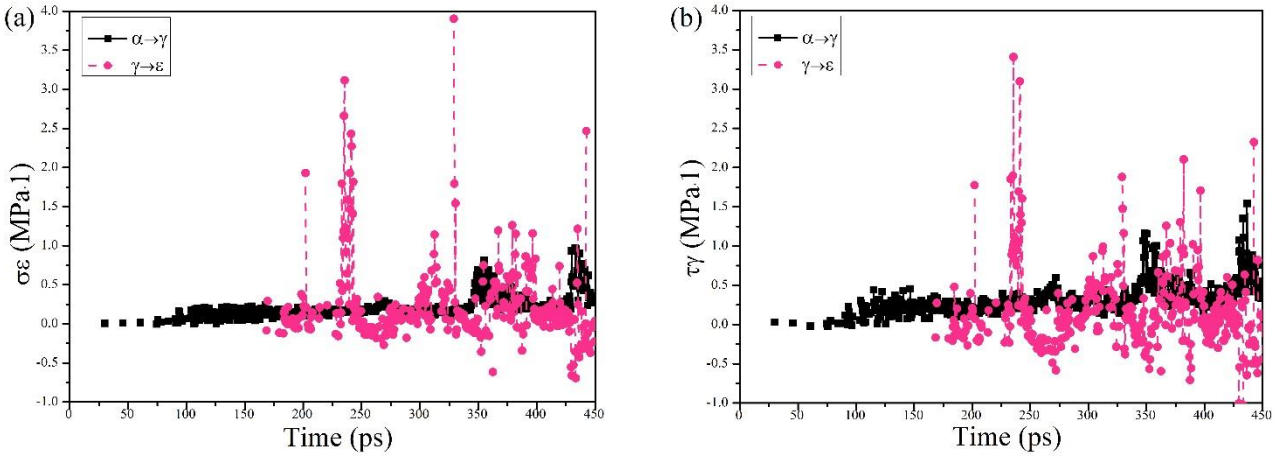

Fig. 11. Components of mechanical driving force for phase transformation. (a) a component of volume for α→γ which is larger than 0， but for γ→ε which usually less than 0, indicating that ε phase is unstable. (b) a component for shear, for α→γ which is almost larger than 0, but for γ→ε which usually less than 0, indicating that ε phase is unstable.

By applying Eq.(8), the calculated components of driving forces for the effect of volume and shear tension are illustrated in Fig. 11. It could be seen that both $\sigma\delta$ and $\tau\gamma$ were larger than 0 once the γ phase is formed, which indicates that the volumetric change affected by both the principal stress and shearing is beneficial to the α→γ transformation. Although they are very high when the ε phase is formed, both driving forces for γ→ε transformation are fluctuated greatly and stayed minus most of the time. This phenomenon suggestes that the smaller amount of the ε phase is formed due to the instability of stacking faults in the γ phase. This is consistent with experimental observations and first-principle calculations that a stable ε phase of iron always occurs in high pressure [36, 38, 145, 146]. It is also the reason that the ε phase is always an intermediate phase in the γ→α phase transformation in iron and iron alloys [1, 19].

4. Conclusions

By using the MD simulation and first-principle calculations modeling, we have studied the tension process of an α-Fe single crystal specimen with a (010)[100] pre-crack along the [010] direction. An algorithm for tracking the crack tip position is proposed by scanning nearby atoms in MD, from which K_{IC} can be directly calculated with the extrapolation method. This method can reduce the influence of boundary conditions to the simulation system with fewer assumptions. The obtained the results agree with the experimental values in the literature. To summarize, we have reached following conclusions:

1) In our simulation, the strain-induced γ and ε phases are observed in the quasi-cleavage fracture process. Both the volumetric and shear strain has the positive effect on the driving force when the phase transformations occur. Activated shear slips on {112} and {110} planes produce the γ phase at the cross zone of {112}<111> and {110}<111> slip systems. While the occurrence of ε phase depends on the existence of γ phase because this phase forms inside of γ phase as a result of stacking faults.
2) The ε phase embryo is unstable. Although tension makes the strain-induced γ→ε martensitic transformation possible, the growth of the ε phase will be suppressed soon after the nucleation of ε phase due to the decrease of driving force. This is consistent with the first-principle calculations that the equilibrium state of ε phase is obtained under high pressure.
3) During the tensile loading, a few dislocation motions occur at the beginning stage of the crack propagation, after which the plasticity is mainly provided by strain-induced martensitic phase transformations.

Acknowledgments

This work is funded by the National Natural Science Foundation of China (Grant No. 11174030, 51701171). The authors acknowledge the foundation for financial support.

References

1. Fischer FD, Sun QP, Tanaka K (1996) Transformation-Induced Plasticity (TRIP). Appl Mech Rev 49:317–364. https://doi.org/10.1115/1.3101930
2. Fischer FD, Reisner G, Werner E, et al (2000) A new view on transformation induced plasticity (TRIP). Int J Plast 16:723–748. https://doi.org/10.1016/S0749-6419(99)00078-9
3. De Jong M, Rathenau G. (1959) Mechanical properties of iron and some iron alloys while undergoing allotropic transformation. Acta Metall 7:246–253. https://doi.org/10.1016/0001-6160(59)90017-3
4. Giles PM, Longenbach MH, Marder AR (1971) High- Pressure α≓ε Martensitic Transformation in

Iron. J Appl Phys 42:4290–4295. https://doi.org/10.1063/1.1659768

5. Merkel S, Wenk H-R, Gillet P, et al (2004) Deformation of polycrystalline iron up to 30 GPa and 1000 K. Phys Earth Planet Inter 145:239–251. https://doi.org/10.1016/J.PEPI.2004.04.001
6. Olson GB, Cohen M (1972) A mechanism for the strain-induced nucleation of martensitic transformations. J Less Common Met 28:107–118. https://doi.org/10.1016/0022-5088(72)90173-7
7. Zackay VF, Bhandarkar MD, Parker ER (1978) The Role of Deformation-Induced Phase Transformations in the Plasticity of Some Iron-Base Alloys. In: Burke JJ, Weiss V (eds) Advances in Deformation Processing. Springer US, Boston, MA, pp 351–404
8. Taleb L (2014) Transformation-Induced Plasticity (TRIP). In: Hetnarski RB (ed) Encyclopedia of Thermal Stresses. Springer Netherlands, Dordrecht, pp 6153–6163
9. Olson GB, Cohen M (1976) A general mechanism of martensitic nucleation: Part I. General concepts and the FCC → HCP transformation. Metall Trans A 7:1897–1904. https://doi.org/10.1007/BF02659822
10. Olson GB, Cohen M (1976) A general mechanism of martensitic nucleation: Part II. FCC → BCC and other martensitic transformations. Metall Trans A 7:1905–1914. https://doi.org/10.1007/BF02659823
11. Olson GB, Cohen M (1976) A general mechanism of martensitic nucleation: Part III. Kinetics of martensitic nucleation. Metall Trans A 7:1915–1923. https://doi.org/10.1007/BF02659824
12. Yang X-S, Sun S, Zhang T-Y (2015) The mechanism of bcc α′ nucleation in single hcp ε laths in the fcc γ → hcp ε → bcc α′ martensitic phase transformation. Acta Mater 95:264–273. https://doi.org/10.1016/J.ACTAMAT.2015.05.034
13. Yang X-S, Sun S, Ruan H-H, et al (2017) Shear and shuffling accomplishing polymorphic fcc γ → hcp ε → bct α martensitic phase transformation. Acta Mater 136:347–354. https://doi.org/10.1016/J.ACTAMAT.2017.07.016
14. Yang X-S, Sun S, Wu X-L, et al (2014) Dissecting the Mechanism of Martensitic Transformation via Atomic-Scale Observations. Sci Rep 4:6141
15. Mahnken R, Schneidt A, Antretter T (2009) Macro modelling and homogenization for transformation induced plasticity of a low-alloy steel. Int J Plast 25:183–204. https://doi.org/10.1016/J.IJPLAS.2008.03.005
16. Fischlschweiger M, Cailletaud G, Antretter T (2012) A mean-field model for transformation induced plasticity including backstress effects for non-proportional loadings. Int J Plast 37:53–71.

https://doi.org/10.1016/J.IJPLAS.2012.04.001

17. Lischka FT, de Oliveira CAS (2015) The study of TRIP effect in an austenitic stainless steel AISI 304 . J Achiev Mater Manuf Eng 71:34
18. Petit B, Gey N, Cherkaoui M, et al (2007) Deformation behavior and microstructure/texture evolution of an annealed 304 AISI stainless steel sheet. Experimental and micromechanical modeling. Int J Plast 23:323–341. https://doi.org/10.1016/J.IJPLAS.2006.07.002
19. Hedström P (2007) Deformation and martensitic phase transformation in stainless steels. Luleå tekniska universitet
20. Du C, Hoefnagels JPM, Kölling S, et al (2018) Martensite crystallography and chemistry in dual phase and fully martensitic steels. Mater Charact 139:411–420. https://doi.org/10.1016/J.MATCHAR.2018.03.011
21. Xiao J (2006) The Metallography of stainless Steel, 2nd ed. Metallurgical Industry Press, Beijing
22. Sakuma Y, Matsumura O, Takechi H (1991) Mechanical properties and retained austenite in intercritically heat-treated bainite-transformed steel and their variation with Si and Mn additions. Metall Trans A 22:489–498. https://doi.org/10.1007/BF02656816
23. Timokhina IB, Hodgson PD, Pereloma E V (2004) Effect of microstructure on the stability of retained austenite in transformation-induced-plasticity steels. Metall Mater Trans A 35:2331–2341. https://doi.org/10.1007/s11661-006-0213-9
24. Tian Y, Lin S, Ko JYP, et al (2018) Micromechanics and microstructure evolution during in situ uniaxial tensile loading of TRIP-assisted duplex stainless steels. Mater Sci Eng A 734:281–290. https://doi.org/10.1016/J.MSEA.2018.07.040
25. Ennis BL, Jimenez-Melero E, Atzema EH, et al (2017) Metastable austenite driven work-hardening behaviour in a TRIP-assisted dual phase steel. Int J Plast 88:126–139. https://doi.org/10.1016/J.IJPLAS.2016.10.005
26. Choi, I.D (2002) Deformation behavior of low carbon TRIP sheet steels at high strain rates. Tetsu- to-Hagane 88:A35
27. Matsumura O, Sakuma Y, Takechi H (1992) Retained Austenite in 0.4C-Si-1.2Mn Steel Sheet Intercritically Heated and Austempered. ISIJ Int 32:1014–1020
28. Matsumura O, Sakuma Y, Takechi H (1987) Enhancement of Elongation by Retained Austenite in Intercritical Annealed 0.4C-1.5Si-O.8Mn Steel. Trans Iron Steel Inst Japan 27:570–579
29. Belonoshko AB, Lukinov T, Fu J, et al (2017) Stabilization of body-centred cubic iron under inner-

core conditions. Nat Geosci 10:312

30. Kalantar DH, Belak JF, Collins GW, et al (2005) Direct observation of the alpha-epsilon transition in shock-compressed iron via nanosecond x-ray diffraction. Phys Rev Lett 95:075502
31. Yaakobi B, Boehly TR, Meyerhofer DD, et al (2005) EXAFS measurement of iron bcc-to-hcp phase transformation in nanosecond-laser shocks. Phys Rev Lett 95:075501
32. Wenk H-R, Matthies S, Hemley RJ, et al (2000) The plastic deformation of iron at pressures of the Earth's inner core . Nature 405:1044–1047. https://doi.org/10.1038/35016558
33. Jeanloz R, Wenk H-R (1988) Convection and anisotropy of the inner core. Geophys Res Lett 15:72–75. https://doi.org/10.1029/GL015i001p00072
34. Burgers WG (1934) On the process of transition of the cubic-body-centered modification into the hexagonal-close-packed modification of zirconium. Physica 1:561–586. https://doi.org/10.1016/S0031-8914(34)80244-3
35. Johnson DF, Carter EA (2008) Nonadiabaticity in the iron bcc to hcp phase transformation. J Chem Phys 128:104703
36. Lu Z, Zhu W, Lu T, Wang W (2014) Does the fcc phase exist in the Fe bcc-hcp transition? A conclusion from first-principles studies. Model Simul Mater Sci Eng 22:25007. https://doi.org/10.1088/0965-0393/22/2/025007
37. Wang FM, Ingalls R (1998) Iron BCC-HCP transition: local structure from x-ray-absorption fine structure. Phys Rev B (Condensed Matter) 57:5647–5654
38. Kadau K, Germann TC, Lomdahl PS, Holian BL (2005) Atomistic simulations of shock-induced transformations and their orientation dependence in bcc Fe single crystals. Phys Rev B 72:064120
39. Latapie A, Farkas D (2003) Molecular dynamics simulations of stress-induced phase transformations and grain nucleation at crack tips in Fe. Model Simul Mater Sci Eng 11:745–753. https://doi.org/10.1088/0965-0393/11/5/303
40. Wang BT, Shao JL, Zhang GC, et al (2009) Molecular dynamics simulations of hcp/fcc nucleation and growth in bcc iron driven by uniaxial compression. J Phys Condens Matter 21:495702. https://doi.org/10.1088/0953-8984/21/49/495702
41. Ivanisenko Y, MacLaren I, Sauvage X, et al (2006) Shear-induced $\alpha \rightarrow \gamma$ transformation in nanoscale Fe–C composite. Acta Mater 54:1659–1669. https://doi.org/10.1016/J.ACTAMAT.2005.11.034
42. Amram D, Kovalenko O, Rabkin E (2015) The $\alpha \leftrightarrow \gamma$ transformation in Fe and Fe–Au thin films, micro- and nanoparticles – an in situ study. Acta Mater 98:343–354.

https://doi.org/10.1016/J.ACTAMAT.2015.07.051

43. Sandoval L, Urbassek HM, Entel P (2009) The Bain versus Nishiyama-Wassermann path in the martensitic transformation of Fe. New J Phys 11:103027. https://doi.org/10.1088/1367-2630/11/10/103027
44. Sandoval L, Urbassek HM (2009) Solid-solid phase transitions in Fe nanowires induced by axial strain. Nanotechnology 20:325704. https://doi.org/10.1088/0957-4484/20/32/325704
45. Wang B, Urbassek HM (2013) Computer simulation of strain-induced phase transformations in thin Fe films. Model Simul Mater Sci Eng 21:85007. https://doi.org/10.1088/0965-0393/21/8/085007
46. Wang B, Sak-Saracino E, Sandoval L, Urbassek HM (2014) Martensitic and austenitic phase transformations in Fe-C nanowires. Model Simul Mater Sci Eng 22:45003. https://doi.org/10.1088/0965-0393/22/4/045003
47. Sih GC, Liebowitz H (1968) Mathematical Theories of Brittle Fracture. In: Liebowitz H (ed) Fracture: An advanced treatise. Academic Press, New York, pp 68–191
48. Kohlhoff S, Gumbsch P, Fischmeister HF (1991) Crack propagation in b.c.c. crystals studied with a combined finite-element and atomistic model. Philos Mag A 64:851–878. https://doi.org/10.1080/01418619108213953
49. Plimpton S (1995) Fast Parallel Algorithms for Short-Range Molecular Dynamics. J Comput Phys 117:1–19. https://doi.org/10.1006/JCPH.1995.1039
50. Mendelev MI, Han S, Srolovitz DJ, et al (2003) Development of new interatomic potentials appropriate for crystalline and liquid iron. Philos Mag 83:3977–3994. https://doi.org/10.1080/14786430310001613264
51. Ramasubramaniam A, Itakura M, Carter EA (2010) Interatomic potentials for hydrogen in alpha-iron based on density functional theory. Phys Rev B 81:099902
52. Allen MP, Tildesley DJ, Banavar JR (1987) Computer Simulation of Liquids. Oxford University Press, New York,US
53. Lawn BR (2010) Fracture of brittle solids, 2nd ed. Cambridge University Press & Higher Education Press, Beijing,China
54. Shinoda W, Shiga M, Mikami M (2004) Rapid estimation of elastic constants by molecular dynamics simulation under constant stress. Phys Rev B 69:1341031
55. Parrinello M, Rahman A (1982) Strain fluctuations and elastic constants. J Chem Phys 76:2662–2666
56. Stukowski A, Bulatov V V, Arsenlis A (2012) Automated identification and indexing of dislocations

in crystal interfaces. Model Simul Mater Sci Eng 20:85007. https://doi.org/10.1088/0965-0393/20/8/085007

57. Stukowski A (2012) Structure identification methods for atomistic simulations of crystalline materials. Model Simul Mater Sci Eng 20:45021. https://doi.org/10.1088/0965-0393/20/4/045021
58. Shimizu F, Ogata S, Li J (2007) Theory of shear banding in metallic glasses and molecular dynamics calculations. Mater Trans 48:2923–2927
59. Stukowski A (2010) Visualization and analysis of atomistic simulation data with OVITO -- The Open Visualization Tool
60. Momma K, Izumi F (2011) VESTA3 for three-dimensional visualization of crystal, volumetric and morphology data. J Appl Crystallogr 44:1272–1276. https://doi.org/10.1107/S0021889811038970
61. Oliphant T (2006) NumPy: A guide to NumPy. http://www.numpy.org/
62. Jones E, Oliphant T, Peterson P, Others (2001) SciPy: Open source scientific tools for Python. http://www.scipy.org/
63. Coleman SP, Sichani MM, Spearot DE (2014) A Computational Algorithm to Produce Virtual X-ray and Electron Diffraction Patterns from Atomistic Simulations. JOM 66:408–416. https://doi.org/10.1007/s11837-013-0829-3
64. Coleman SP, Pamidighantam S, Van Moer M, et al (2014) Performance Improvement and Workflow Development of Virtual Diffraction Calculations. In: Proceedings of the 2014 Annual Conference on Extreme Science and Engineering Discovery Environment. ACM, New York, NY, USA, pp 61:1--61:7
65. Childs H, Brugger E, Whitlock B, et al (2016) VisIt: An End-User Tool For Visualizing and Analyzing Very Large Data. In: Bethel EW, Childs H, Hansen C (eds) High Performance Visualization:Enabling Extreme-Scale Scientific Insight. CRC Press, Taylor & Francis Group, Boca; Raton; London; New York, pp 357–372
66. Barber CB, Dobkin DP, Dobkin DP, Huhdanpaa H (1996) The Quickhull Algorithm for Convex Hulls. ACM Trans Math Softw 22:469–483. https://doi.org/10.1145/235815.235821
67. Rafii-Tabar H, Hua L, Cross M (1998) A multi-scale atomistic-continuum modelling of crack propagation in a two-dimensional macroscopic plate. J Phys Condens Matter 10:2375–2387. https://doi.org/10.1088/0953-8984/10/11/003
68. Rafii-Tabar H, Shodja HM, Darabi M, Dahi A (2006) Molecular dynamics simulation of crack propagation in fcc materials containing clusters of impurities. Mech Mater 38:243–252.

https://doi.org/10.1016/J.MECHMAT.2005.06.006

69. Hua L, RAFII-TABAR H, Cross M (1997) Molecular dynamics simulation of fractures using an N-body potential. Philos Mag Lett 75:237–244. https://doi.org/10.1080/095008397179480
70. Chandra S, Kumar NN, Samal MK, et al (2016) Molecular dynamics simulations of crack growth behavior in Al in the presence of vacancies. Comput Mater Sci 117:518–526. https://doi.org/10.1016/J.COMMATSCI.2016.02.032
71. Petucci JM (2013) A Study of Crack Propagation in Metals in the Presence of Defects.PhD Dissertation. Indiana University of Pennsylvania
72. Ding J, Wang L, Song K, et al (2017) Molecular Dynamics Simulation of Crack Propagation in Single-Crystal Aluminum Plate with Central Cracks. J Nanomater 2017:12. https://doi.org/10.1155/2017/5181206
73. Xie D, Qian Q, Li C (2009) Numerical calculation methods and Engineering Application in fracture Mechanics. Science Press, Beijing
74. Rooke DP, Cartwright DJ (1976) Compendium of stress intensity factors. Her Majesty's Stationery Office, The Hillingdon Press, London
75. Irwin GR (1957) Analysis of Stresses and Strains near the End of a Crack Traversing a Plate. J Appl Mech ASME E24:351–369
76. Tsai DH (1979) The virial theorem and stress calculation in molecular dynamics. J Chem Phys 70:1375–1382
77. Fung YC (1977) A first course in continuum mechanics, 2nd editio. Prentice-Hall, Inc., Englewood Cliffs
78. Kresse G, Furthmüller J (1996) Efficiency of ab-initio total energy calculations for metals and semiconductors using a plane-wave basis set. Comput Mater Sci 6:15–50. https://doi.org/https://doi.org/10.1016/0927-0256(96)00008-0
79. Kresse G (1995) Ab initio molecular dynamics for liquid metals. J Non Cryst Solids 192–193:222–229. https://doi.org/https://doi.org/10.1016/0022-3093(95)00355-X
80. Kresse G, Hafner J (1994) Ab initio molecular-dynamics simulation of the liquid-metal-amorphous-semiconductor transition in germanium. Phys Rev B Condens Matter 49:14251
81. Kresse G (1993) Ab initio molecular dynamics for liquid metals. Phys Rev B Condens Matter 48:13115–13118
82. Perdew JP, Burke K, Ernzerhof M (1998) ERRATA:Generalized gradient approximation made

simple. Phys Rev Lett 77:3865–3868

83. Perdew JP, Burke K, Ernzerhof M (1996) Generalized gradient approximation made simple. Phys Rev Lett 77:3865–3868. https://doi.org/10.1103/PhysRevLett.77.3865
84. Blöchl PE (1994) Projector augmented-wave method. Phys Rev B 50:17953–17979
85. Kresse G, Joubert D (1999) From ultrasoft pseudopotentials to the projector augmented-wave method. Phys Rev B 59:1758–1775. https://doi.org/10.1103/PhysRevB.59.1758
86. Monkhorst HJ, Pack JD (1976) Special points for Brillouin-zone integrations. Phys Rev B 13:5188–5192. https://doi.org/10.1103/PhysRevB.13.5188
87. Wang V, Xu N (2019) VASPKIT: A Pre- and Post-Processing Program for the VASP Code. http://vaspkit.sourceforge.net
88. Birch F (1947) Finite Elastic Strain of Cubic Crystals. Phys Rev 71:809–824. https://doi.org/10.1103/PhysRev.71.809
89. Murnaghan FD (1944) The Compressibility of Media under Extreme Pressures. Proc Natl Acad Sci U S A 30:244–7. https://doi.org/10.1073/pnas.30.9.244
90. Merkel S, Liermann H-P, Miyagi L, Wenk H-R (2013) In situ radial X-ray diffraction study of texture and stress during phase transformations in bcc-, fcc- and hcp-iron up to 36 GPa and 1000 K. Acta Mater 61:5144–5151. https://doi.org/10.1016/J.ACTAMAT.2013.04.068
91. Iglesias R, Palacios SL (2007) Ab initio studies on the magnetic phase stability of iron. Acta Mater 55:5123–5127. https://doi.org/10.1016/J.ACTAMAT.2007.05.035
92. Tsetseris L (2005) Noncollinear magnetism of iron along the tetragonal Bain transformation. Phys Rev B - Condens Matter Mater Phys 72:2–5. https://doi.org/10.1103/PhysRevB.72.012411
93. Zhang X, Hickel T, Rogal J, Neugebauer J (2016) Interplay between interstitial displacement and displacive lattice transformations. Phys Rev B 94:1–9. https://doi.org/10.1103/PhysRevB.94.104109
94. Okatov S V., Kuznetsov AR, Gornostyrev YN, et al (2009) Effect of magnetic state on the $\gamma - \alpha$ transition in iron: First-principles calculations of the Bain transformation path. Phys Rev B 79:094111. https://doi.org/10.1103/PhysRevB.79.094111
95. Medvedeva NI, Van Aken D, Medvedeva JE (2010) Magnetism in bcc and fcc Fe with carbon and manganese. J Phys Condens Matter 22:. https://doi.org/10.1088/0953-8984/22/31/316002
96. Steinle-Neumann G, Stixrude L, Cohen RE (2004) Magnetism in dense hexagonal iron. Proc Natl Acad Sci U S A 101:33–6. https://doi.org/10.1073/pnas.2237239100
97. Schultz RA, Jensen MC, Bradt RC (1994) Single crystal cleavage of brittle materials. Int J Fract

65:291–312. https://doi.org/10.1007/BF00012370

98. Huang C, Peng X, Yang B, et al (2017) Investigation of Interaction between Dislocation Loop and Coherent Twin Boundary in BCC Ta Film during Nanoindentation. Nanomaterials 7:. https://doi.org/10.3390/nano7110375
99. Li D, Wang F, Yang Z, Zhao Y (2014) How to identify dislocations in molecular dynamics simulations? Sci China Physics, Mech Astron 57:2177–2187. https://doi.org/10.1007/s11433-014-5617-8
100. Farkas D (2000) Atomistic Studies of Intrinsic Crack-Tip Plasticity. MRS Bull 25:35–38. https://doi.org/10.1557/mrs2000.71
101. Li D, Meng FY, Ma XQ, et al (2011) Molecular Dynamics Simulation of Porous Layer-enhanced Dislocation Emission and Crack Propagation in Iron Crystal. J Mater Sci Technol 27:1025–1028. https://doi.org/10.1016/S1005-0302(11)60181-3
102. Song J, Soare M, Curtin WA (2010) Testing continuum concepts for hydrogen embrittlement in metals using atomistics. Model Simul Mater Sci Eng 18:45003. https://doi.org/10.1088/0965-0393/18/4/045003
103. Gordon PA, Neeraj T, Luton MJ, Farkas D (2007) Crack-Tip Deformation Mechanisms in α-Fe and Binary Fe Alloys: An Atomistic Study on Single Crystals. Metall Mater Trans A 38:2191–2202. https://doi.org/10.1007/s11661-007-9176-8
104. Sakaki T, Nakamura T (1973) Cleavage Fracture of Iron Single Crystals. Tetsu-to-Hagane 59:955–966. https://doi.org/10.2355/tetsutohagane1955.59.7_955
105. Hribernik ML (2006) Cleavage oriented iron single crystal fracture toughness.PhD Dissertation. University of California, Santa Barbara
106. Chen JH, Cao R (2015) Introduction. In: Chen JH, Cao R (eds) Micromechanism of Cleavage Fracture of Metals:A Comprehensive Microphysical Model for Cleavage Cracking in Metals. Butterworth-Heinemann, pp 1–54
107. Chang L, Zhou C-Y, Wen L-L, et al (2017) Molecular dynamics study of strain rate effects on tensile behavior of single crystal titanium nanowire. Comput Mater Sci 128:348–358. https://doi.org/10.1016/J.COMMATSCI.2016.11.034
108. Dong Q, Zai S, Sun J, Liu M (2011) Tensile Test Rate and Its Control in GB/T228.1-2010 Standard. Phys Test Chem Anal Part A(Physical Testing) 47:774–781
109. Koh SJA, Lee HP, Lu C, Cheng QH (2005) Molecular dynamics simulation of a solid platinum

nanowire under uniaxial tensile strain: Temperature and strain-rate effects. Phys Rev B 72:085414

110. Ingram TG (1934) The mechanism of plastic deformation of crystals. Part I.—Theoretical. Proc R Soc London Ser A, Contain Pap a Math Phys Character 145:362–387. https://doi.org/10.1098/rspa.1934.0106
111. John VB (1990) Defects in Crystals and Plastic Deformation BT - Engineering Materials. In: John VB (ed). Macmillan Education UK, London, pp 41–57
112. Dobromyslov A V, Kozlov EA, Taluts NI (2008) High-strain-rate deformation of armco iron induced by spherical and quasi-spherical converging shock waves and the mechanism of the α-ε transformation. Phys Met Metallogr 106:531–541. https://doi.org/10.1134/S0031918X08110136
113. Cottrell AH (1958) THEORY OF BRITTLE FRACTURE IN STEEL SIMILAR METALS. Trans Metall Soc AIME 212:192–203
114. Möller JJ, Bitzek E (2014) Comparative study of embedded atom potentials for atomistic simulations of fracture inα-iron. Model Simul Mater Sci Eng 22:45002. https://doi.org/10.1088/0965-0393/22/4/045002
115. Song J, Curtin WA (2012) Atomic mechanism and prediction of hydrogen embrittlement in iron. Nat Mater 12:145
116. Guo Y-F, Wang Y-S, Zhao D-L (2007) Atomistic simulation of stress-induced phase transformation and recrystallization at the crack tip in bcc iron. Acta Mater 55:401–407. https://doi.org/10.1016/J.ACTAMAT.2006.08.022
117. Becquart CS, Kim D, Rifkin JA, Clapp PC (1993) Fracture properties of metals and alloys from molecular dynamics simulations. Mater Sci Eng A 170:87–94. https://doi.org/10.1016/0921-5093(93)90371-K
118. Matsumoto R, Taketomi S, Matsumoto S, Miyazaki N (2009) Atomistic simulations of hydrogen embrittlement. Int J Hydrogen Energy 34:9576–9584. https://doi.org/10.1016/J.IJHYDENE.2009.09.052
119. Garrison WM, Moody NR (1987) Ductile fracture. J Phys Chem Solids 48:1035–1074. https://doi.org/10.1016/0022-3697(87)90118-1
120. Sandoval L, Urbassek HM (2009) Transformation pathways in the solid-solid phase transitions of iron nanowires. Appl Phys Lett 95:191909. https://doi.org/10.1063/1.3258002
121. Hui X, Chen G (2007) Bulk metallic glass alloys. Chemical Industry Press, Beijing
122. Ikeda H, Qi Y, Ifmmode Mbox C C Else C C Fi Agin T, et al (1999) Strain Rate Induced

Amorphization in Metallic Nanowires. Phys Rev Lett 82:2900–2903

123. Haberl B, Bradby JE, Swain M V., et al (2004) Phase transformations induced in relaxed amorphous silicon by indentation at room temperature. Appl Phys Lett 85:5559–5561. https://doi.org/10.1063/1.1832757

124. Lew A, Caspersen K, Carter EA, Ortiz M (2006) Quantum mechanics based multiscale modeling of stress-induced phase transformations in iron. J Mech Phys Solids 54:1276–1303. https://doi.org/10.1016/J.JMPS.2005.11.009

125. Steinle-Neumann G, Stixrude L, Cohen RE (1999) First-principles elastic constants for the hcp transition metals Fe, Co, and Re at high pressure. Phys Rev B Condens Matter 60:791–799

126. Caspersen KJ, Lew A, Ortiz M, Carter EA (2004) Importance of Shear in the bcc-to-hcp Transformation in Iron. Phys Rev Lett 93:115501

127. Zarkevich NA, Johnson DD (2015) Coexistence pressure for a martensitic transformation from theory and experiment: Revisiting the bcc-hcp transition of iron under pressure. Phys Rev B 91:174104

128. Mao W (2007) Structure Principles of Crystalline Materials. Metallurgical Industry Press, Beijing

129. Patel JR, Cohen M (1953) Criterion for the action of applied stress in the martensitic transformation. Acta Metall 1:531–538. https://doi.org/10.1016/0001-6160(53)90083-2

130. Murata Y (2018) Formation Mechanism of Lath Martensite in Steels. Mater Trans 59:151–164. https://doi.org/10.2320/matertrans.M2016430

131. Anderson OL, Runcorn SK, Creer KM, Jacobs JA (1982) The Earth's core and the phase diagram of iron. Philos Trans R Soc London Ser A, Math Phys Sci 306:21–35

132. Spitzig WA, Keh AS (1970) Orientation and temperature dependence of slip in iron single crystals. Metall Trans 1:2751. https://doi.org/10.1007/BF03037811

133. Opinsky AJ, Smoluchowski R (1951) The Crystallographic Aspect of Slip in Body- Centered Cubic Single Crystals. I. Theoretical Considerations. J Appl Phys 22:1380–1384. https://doi.org/10.1063/1.1699870

134. Allen NP, Hopkins BE, McLennan JE, Bullard EC (1956) The tensile properties of single crystals of high-purity iron at temperatures from 100 to -253°C. Proc R Soc London Ser A Math Phys Sci 234:221–246

135. Ingram TG, F. EC (1926) The distortion of iron crystals. Proc R Soc London Ser A, Contain Pap a Math Phys Character 112:337–361. https://doi.org/10.1098/rspa.1926.0116

136. Lim H, Weinberger CR, Battaile CC, Buchheit TE (2013) Application of generalized non-Schmid

yield law to low-temperature plasticity in bcc transition metals. Model Simul Mater Sci Eng 21:45015. https://doi.org/10.1088/0965-0393/21/4/045015

137. Ou X, Song M (2019) Deformation mechanisms of mechanically induced phase transformations in iron. Comput Mater Sci 162:12–20. https://doi.org/10.1016/J.COMMATSCI.2019.02.028
138. Humphreys FJ, Hatherly M, Humphreys FJ, Hatherly M (2004) The Deformed State. Recryst Relat Annealing Phenom 11–II. https://doi.org/10.1016/B978-008044164-1/50006-2
139. Bryukhanova KI, Nikiforova GE, Tyurin A V, et al (2018) The heat capacity of LaPO4 and PrPO4 nanowhiskers. J Therm Anal Calorim 132:337–342. https://doi.org/10.1007/s10973-017-6593-9
140. Wilson GG, H. JR, Leonard R (1965) The deformation of metals under small stresses during phase transformations. Proc R Soc London Ser A Math Phys Sci 283:403–422. https://doi.org/10.1098/rspa.1965.0029
141. Magee CL, Paxton HW (1966) Transformation kinetics, microplasticity and aging of martensite in Fe-31Ni.PhD Dissertation. Carnegie Institute of Technology
142. Fischlschweiger M, Cailletaud G, Antretter T (2012) A mean-field model for transformation induced plasticity including backstress effects for non-proportional loadings. Int J Plast 37:53–71. https://doi.org/10.1016/J.IJPLAS.2012.04.001
143. Mahnken R, Schneidt A, Antretter T (2009) Macro modelling and homogenization for transformation induced plasticity of a low-alloy steel. Int J Plast 25:183–204. https://doi.org/10.1016/J.IJPLAS.2008.03.005
144. L. Fischer L, E. Beltz G (2001) The effect of crack blunting on the competition between dislocation nucleation and cleavage. J Mech Phys Solids 49:635–654. https://doi.org/10.1016/S0022-5096(00)00042-9
145. Herper HC, Hoffmann E, Entel P (1999) Ab initio full-potential study of the structural and magnetic phase stability of iron. Phys Rev B 60:3839–3848
146. Tateno S, Hirose K, Ohishi Y, Tatsumi Y (2010) The structure of iron in Earth's inner core. Science (80-) 330:359–61. https://doi.org/10.1126/science.1194662